Ocean Sci. Discuss., 6, 2755–2829, 2009
www.ocean-sci-discuss.net/6/2755/2009/

Ocean Science Discussions

This discussion paper is/has been under review for the journal Ocean Science (OS).
Please refer to the corresponding final paper in OS if available.

Sediment $^{231}Pa/^{230}Th$ as a recorder of the rate of the Atlantic meridional overturning circulation: insights from a 2-D model

Y. Luo, R. Francois, and S. E. Allen

Department of Earth and Ocean Sciences, University of British Columbia, 6339 Stores Road, Vancouver, BC, V6T 1Z4, Canada

Received: 3 October 2009 – Accepted: 8 October 2009 – Published: 24 November 2009

Correspondence to: R. Francois (rfrancoi@eos.ubc.ca)

Published by Copernicus Publications on behalf of the European Geosciences Union.

Abstract

A two dimensional scavenging-circulation model is used to investigate the patterns of sediment $^{231}Pa/^{230}Th$ generated by the Atlantic Meridional Overturning Circulation (AMOC) and further advance the application of this proxy for ocean paleocirculation studies. The scavenging parameters and the geometry of the overturning circulation cell have been chosen so that the model generates meridional sections of dissolved ^{230}Th and ^{231}Pa consistent with published water column profiles and an additional 12 previously unpublished profiles measured in the North and Equatorial Atlantic. The processes that generate the meridional sections of dissolved and particulate ^{230}Th, dissolved and particulate ^{231}Pa, dissolved and particulate $^{231}Pa/^{230}Th$, and sediment $^{231}Pa/^{230}Th$ are discussed in detail. The results indicate that the relationship between sediment $^{231}Pa/^{230}Th$ at any given site and the overturning circulation is very complex. They clearly show that constraining past changes in the strength and geometry of the AMOC requires an extensive data set and they suggest strategies to maximize information from a limited number of samples.

1 Introduction

Ocean circulation plays an important role in climate control by transferring solar heat from low to high latitudes (Ganachaud and Wunsch, 2000). In particular, rapid changes in the strength and geometry of the Atlantic Meridional Overturning Circulation (AMOC) have been invoked to explain the abrupt variations in climate that have punctuated the last ice age and deglaciation (Schmittner et al., 2002; Clark et al., 2002). However, documenting the link between changes in climate and ocean circulation still remains a major challenge in paleoclimatology (Lynch-Stieglitz et al., 2007). Past changes in circulation were first inferred from the sedimentary records of nutrient proxies (Boyle and Keigwin, 1987). While these tracers provide important information on changes in the geometry of the overturning circulation, they do not constrain changes in the rate of

OSD

6, 2755–2829, 2009

overturning (Legrand and Wunsch, 1995). To address this problem, several kinematic tracers of ocean circulation are being investigated (Lynch-Stieglitz et al., 2007). The ^{231}Pa/^{230}Th ratio of Atlantic sediments is one of these tracers. This proxy has recently been used to investigate past changes in the rate of the AMOC from the last glacial maximum to present (McManus et al., 2004; Hall et al., 2006; Gherardi et al., 2005; 2009). Because both ^{231}Pa and ^{230}Th have uniform production rates (from the decay of dissolved uranium) and ^{231}Pa has a longer residence time than ^{230}Th in the water column, the AMOC exports ^{231}Pa more effectively from the Atlantic into the Southern Ocean (Yu et al., 1996; Francois, 2007). The modern rate of overturning results in the mean residence time of deep water in the Atlantic roughly equivalent to the mean residence time of ^{231}Pa in the water column (~200years), so that nearly half of the ^{231}Pa produced in Atlantic water is exported to the southern ocean with the water in which it formed. On the other hand, with its much shorter residence time (~30years), nearly all of the ^{230}Th produced in this water is removed into the sediments of the Atlantic and little is exported to the Southern Ocean. As a result, the ^{231}Pa/^{230}Th ratio in Atlantic sediments is about half the production rate ratio of these two isotopes in the water column (0.092 dpm/dpm). Faster rates of overturning export a larger fraction of ^{231}Pa and further decrease ^{231}Pa/^{230}Th, while slower rates of overturning increase this ratio (Marchal et al., 2000).

Application of this simple principle is, however, complicated by two factors. First, sedimentary ^{231}Pa/^{230}Th is not only controlled by the rate of overturning, but also by the removal rate of the two isotopes from the water column by particle scavenging. Scavenging rates, which are controlled by the flux and composition of settling particles (Bacon, 1988; Walter et al., 1997; Chase et al., 2002, 2003), dictate the residence time of ^{231}Pa in seawater and the extent to which it can be exported from the Atlantic by the AMOC (Yu et al., 1996). On the other hand, ^{230}Th has a residence time sufficiently short to severely limit its redistribution by circulation and mixing, even when the rate of overturning is fast (Francois et al., 2004). It is possible to assess the impact of changes in particle scavenging by analyzing the composition of the sediment, which

informs us of changes in particle flux and composition at the site of study and their possible overprint on sediment ^{231}Pa/^{230}Th at this location (Gherardi et al., 2009), at least to the extent that we can take into account the effect of diagenesis. However, the extent to which scavenging can also affect sediment ^{231}Pa/^{230}Th further "downstream" in the overturning circulation cell still needs to be investigated. The second point of contention is the extent to which sediment ^{231}Pa/^{230}Th integrates circulation rates over the overlying water column. In a recent study using a 1-D scavenging model, Thomas et al. (2006) have argued that sedimentary ^{231}Pa/^{230}Th may only record overturning occurring in about 1000 m of water overlying the analyzed sediment and shallower overturning cannot be recorded in deep sediments. We have developed a simple 2-D scavenging-circulation model to revisit these two questions and further explore the factors that affect the distribution of ^{231}Pa/^{230}Th in Atlantic sediments.

2 Model descriptions

Water column profiles of dissolved and particulate ^{230}Th and ^{231}Pa concentration indicate that these two isotopes are removed from seawater by reversible scavenging (Bacon and Anderson, 1982; Nozaki et al., 1987). We use the same formalism to describe scavenging imbedded in a 2-D circulation scheme to investigate how the concentration of ^{231}Pa and ^{230}Th in the water column and sediments can potentially be affected by changes in circulation and scavenging rate.

2.1 Formulation

The scavenging model used for both ^{231}Pa and ^{230}Th is shown in Fig. 1. Dissolved ^{230}Th and ^{231}Pa concentrations (X_d; where X represents ^{230}Th or ^{231}Pa) are controlled by the production rates of the respective nuclides (P_X; dpm m^{-3} y^{-1}), their adsorption (K_1^X) and desorption (K_{-1}^X) rate constants (y^{-1}), and the transport rates imposed by the circulation model (V; m y^{-1}), while ^{230}Th and ^{231}Pa particulate concentrations (X_p) are

controlled by the adsorption/desorption rate constants, transport rates and the sinking rates (S; my^{-1}) of the particles that scavenge the two nuclides from the water column. At steady-state, we can write:

$$d[X]_d/dt = 0 = P_x - K_{1x}[X]_d + K_{-1x}[X]_p + V\Delta[X]_d \quad (1)$$

$$d[X]_p/dt = 0 = K_{1x}[X]_d - K_{-1x}[X]_p + V\Delta[X]_p + d\mathrm{Flux}/dZ \quad (2)$$

$$\mathrm{Flux} = [X]_p S \quad (3)$$

Where X represents ^{230}Th or ^{231}Pa and Z is water depth (m) and Δ is an "upwind" difference divided by the grid spacing (Press et al., 1992). The model uses a uniform grid with a horizontal grid spacing of 2.5 degrees latitude and a vertical grid spacing of 250 m.

These equations are used to calculate the concentration of dissolved and particulate ^{230}Th and ^{231}Pa as a function of depth and latitude.

2.2 Overturning circulation

The 2-D meridional overturning circulation scheme (control run) used in this study is ascribed within a meridional section in the Atlantic Ocean (constant depth of 5000 m from 70° N to 70° S). It consists of two meridional overturning cells flowing in opposite directions (Fig. 2). The Atlantic Meridional Overturning Circulation (AMOC) is initiated by the formation of 20.5 Sv of North Atlantic Deep Water (NADW) (Friedrichs and Hall, 1993; Macdonald, 1998; Talley et al., 2003) resulting from water flowing north in the upper 1500 m of the water column and sinking between 60° N and 70° N. This latitudinal range coincides roughly to the latitudes where deep water forms in the Labrador and Nordic seas. The site of deep water formation (60–70° N) is represented by one homogenized region between 250 to 4250 m depth to represent rapid deep water convection. Water from this homogeneous region is then transported horizontally to the south at different rates (Fig. 2b). The depth distribution of lateral transport was chosen so that the model generates dissolved ^{230}Th and ^{231}Pa profiles consistent with observations (see

OSD
6, 2755–2829, 2009

below). At 10° N, the NADW flow increases to 22.5 Sv with the addition of 2 Sv from the Antarctic Bottom Water (AABW) between 10° N and 35° N. Two Sv of AABW water are added further south, resulting in a total flow of 24.5 Sv of NADW, which is close to the NADW strength (23±3 Sv) estimated from the World Ocean Circulation Experiment (WOCE) data (Ganachaud and Wunsch, 2000). NADW starts to gradually upwell at 37.5° S towards a mixing zone (i.e. one homogeneous region) located above 1000 m between 67.5 and 57.5° S. Water from this mixing zone feeds surface and intermediate water forming the shallow return limb of the AMOC.

The second overturning cell is initiated by 8 Sv of AABW, originating from the same mixing cell, flowing into the southernmost region (67.5–70° S) and sinking directly to 3500 m. Four Sv are transported northward between 3500 m and 4500 m depth and entrained in the upwelling NADW south of 40° S. The remaining 4 Sv are transported northward below 4500 m. This northward flow is gradually attenuated by entrainment in the NADW and disappears at 37.5° N, which is roughly consistent with hydrographic observations (Sloyan and Rintoul, 2001). In this study, we do not specifically represent the Antarctic Intermediate Water (AAIW). Although the rate of AAIW formation may affect the ^{231}Pa/^{230}Th of sediment deposited at intermediate depths in the South Atlantic, preliminary model runs indicate that this water mass has little or no effect on the ^{231}Pa/^{230}Th of deep sea sediments.

2.3 Parameterization

Among all the parameters needed to constrain the model shown in Fig. 1, the production rates for ^{230}Th and ^{231}Pa are best known since they are constant and only depend on the well established concentration of ^{234}U and ^{235}U in seawater (Delanghe et al., 2002; Robinson et al., 2004). The other parameters, however, are associated with greater variability and uncertainties.

Sinking rate (S): most estimates of the average sinking rate of fine particles (S) obtained from water column profiles of particulate ^{230}Th (e.g. Krishnaswami et al., 1981; Rutgers van der Loeff and Berger, 1993; Scholten et al., 1995; Moran et al., 2001)

OSD
6, 2755–2829, 2009

range between 400–800 my^{-1}. Since there are no clear indications of systematic variability in this parameter, we chose a uniform and intermediate value of 500 my^{-1} (Table 1).

K_1^{Th} and K_{-1}^{Th}: the adsorption (K_1) and desorption (K_{-1}) rate constants for ^{230}Th have been estimated using a reversible scavenging model (Bacon and Anderson, 1982; Nozaki et al., 1987; Clegg and Whitfield, 1991; Clegg et al., 1991) and mostly range from 0.2 to 0.8 y^{-1} for K_1^{Th} and 1 to 3 y^{-1} for K_{-1}^{Th}. We chose values within this range (Table 1) which generate dissolved ^{230}Th profiles broadly consistent with water column profiles measured at several locations in the Atlantic and in the Southern Ocean (Fig. 3, Table 2). K_1^{Th} is lower in the Southern Ocean than in the Atlantic, consistent with the data of Chase et al. (2002). We also used higher K_1^{Th} in the upper 500m to reflect the increase in K_1^{Th} with particle concentrations (Bacon and Anderson, 1982).

K_1^{Pa} and K_{-1}^{Pa}: the adsorption and desorption rate constants for ^{231}Pa are even less constrained and we selected their values so as to obtain dissolved ^{231}Pa concentration profiles (Table 2) and fractionation factors that are also broadly consistent with observations in the field.

The fractionation factor is defined as:

$$F = ([^{231}Pa]_d/[^{230}Th]_d)/([^{231}Pa]_p/[^{230}Th]_p) \quad (4)$$

F has been directly measured in the Atlantic and southern ocean (Walter et al., 1997; Moran et al., 2001; Chase et al., 2002). Particle composition affects the fractionation factor (F) due to the stronger affinity of opal for ^{231}Pa. In carbonate dominated regions, F is much higher than in opal dominated regions, where F is close to 1. We have adjusted the adsorption and desorption rate constants with latitude (Table 1) to produce systematic variations in the "equilibrium" fractionation factor which broadly reflect the field observations (Moran et al, 2002; Walter et al, 1997; Table 3). The "equilibrium" fractionation factor is the fractionation factor that would be measured if particles were in equilibrium with surrounding seawater. In this case $[X]_p/[X]_d = K_1^X/K_{-1}^X$ and

$F = (K_{-1}^{Pa} K_1^{Th}) / (K_1^{Pa} K_{-1}^{Th})$. As we will discuss below, however, F measured in the field is also affected by particle sinking rates and circulation. The "equilibrium" fractionation factors used in our control run are set at 7.8 in all waters situated north of 42.5° S. Further south, they decrease gradually to reach a minimum of 0.9 south of 50° S.

In order to calculate the transport rates (V; my^{-1}) needed to obtain the desired water transport fluxes (Sv), we fixed the width of the Atlantic basin in our model at 3000 km.

3 Dissolved ^{230}Th and ^{231}Pa water column profiles: data-model comparison

We used water column data (dissolved ^{230}Th and ^{231}Pa profiles; fractionation factors) to constrain the circulation and scavenging parameters in our model. Dissolved ^{230}Th and ^{231}Pa profiles from the North and Equatorial Atlantic (Table 2, Fig. 3) were measured following the ICP-MS isotope dilution method described by Choi et al. (2000). Samples were collected in 1998 (KNORR 159-7), 1999 (ENDEAVOR 328), and 2005 (ENDEAVOR 407). In this section, we present the fit between field data and those generated by our control run and discuss the processes that generate them.

Simple scavenging models using constant S, K_1 and K_{-1} and neglecting circulation predict a linear increase in dissolved and particulate ^{230}Th and ^{231}Pa concentrations versus depth (Bacon and Anderson, 1982; Bacon et al., 1985; Nozaki et al., 1987):

$$X_p = [P_X / S] Z \quad (5)$$

$$X_d = [P_X / K_1] + [(K_{-1} P_X) / (K_1 S)] Z \quad (6)$$

where Z is depth.

However, most ^{230}Th and ^{231}Pa seawater profiles measured in the ocean display significant deviations from linearity because the effect of circulation can rarely be neglected. The dissolved ^{230}Th and ^{231}Pa concentration profiles obtained with our model using the parameters listed in Table 1 also deviate often from linearity and are broadly consistent with observations.

OSD
6, 2755–2829, 2009

The model reproduces reasonably well the water column profiles measured in the Labrador and Norwegian Sea (Fig. 4). Shallow waters entering the Nordic Seas to produce deep water have low ^{230}Th and ^{231}Pa concentrations and deep winter convective mixing results in low and nearly constant concentration profiles. Concentrations are higher at shallow depths and lower in deep waters than predicted by the scavenging model in the absence of vertical mixing. The fit of the modeled ^{230}Th is best with the profiles measured in the Labrador Sea in 1993 (Moran et al., 1997) and in the Norwegian Sea (Moran et al., 1995). The ^{230}Th concentrations measured in the Labrador Sea in 1999 are significantly higher and have been attributed to a temporary cessation of deep water convection in the Labrador Sea during that period (Moran et al., 2002). The build-up of ^{231}Pa resulting from the same effect is expected to be much smaller (the response time is equivalent to the residence time and is longer for ^{231}Pa; see below), and we find a reasonable fit between the model and the 1999 Labrador Sea measurements of dissolved ^{231}Pa (although the model generates somewhat higher concentrations than observed).

The concentration deficit in deep waters generated in the Nordic and Labrador Seas spreads southward with the North Atlantic Deep Water. During transit to the Southern Ocean, the newly formed deep water is continuously subjected to the particle rain that originates from surface waters and which scavenges the ^{230}Th and ^{231}Pa continuously produced in the water column. When particles reach the depth of the newly formed deep water where the ^{230}Th and ^{231}Pa seawater concentrations are below steady-state concentrations dictated by scavenging, desorption from particles is enhanced and a fraction of the ^{230}Th and ^{231}Pa scavenged at shallower depths is released to the deep waters instead of being removed into the underlying sediments. Thus, the ^{230}Th and ^{231}Pa concentrations in newly formed deep waters gradually increase during transit to the southern ocean until the concentration at steady state with respect to scavenging is regained, at which point the water column profiles have relaxed back to linearity (Francois, 2007). The gradual relaxation of the profiles to linearity can be described for each isopycnal by adding a lateral transport term to the scavenging model, as first

OSD
6, 2755–2829, 2009

proposed by Rutgers van der Loeff and Berger (1993):

$$\partial X_t/\partial t = P_X - S\partial(KX_t)/\partial Z + (X_t - {}^{i}X_t)/\tau_w = 0 \quad (7)$$

Where ${}^{i}X_t$ and X_t are total ^{230}Th or ^{231}Pa concentration measured at two locations on the same isopycnal and τ_w is the "transit time" of water between these two sites. In deep waters, $K(=X_p/X_t)$ is nearly constant. Integrating the above equation thus gives:

$$[\mathrm{Th}]_t \cong (P_{\mathrm{Th}}\tau_w + {}^{i}[\mathrm{Th}]_t)(1 - e^{-Z/\tau wSK}) \quad (8)$$

$$[\mathrm{Th}]_t \cong (P_{\mathrm{Th}}\tau_w + {}^{i}[\mathrm{Th}]_t)(1 - e^{-\tau_{\mathrm{scav}}/\tau w}) \quad (9)$$

These equations predict that the radioisotope profiles relax back to linearity with a e-folding time proportional to the residence time of the radioisotope with respect to scavenging ($\tau_{\mathrm{scav}}=Z/SK$). Profile linearity is thus regained faster at shallower depths, where residence times are shorter, and ^{230}Th regains linearity faster than ^{231}Pa because of its shorter residence time in the water column. The shapes of the ^{230}Th profiles measured in the Atlantic are in agreement with this simple conceptual model and are also reproduced in the control run (Figs. 5 and 6). The seawater data show clearly the gradual southward relaxation of the profiles towards linearity. Linearity is regained faster for ^{230}Th and at shallower depths. We also note that the profiles from the western Atlantic display a greater deficit farther south, reflecting the stronger ventilation of the western Atlantic basins. The profiles obtained from the model (Figs. 5c and 6c) show similar trends with dissolved ^{230}Th and ^{231}Pa concentrations close to those observed in the ocean.

Further south, where the deep waters start to upwell, their relatively high ^{230}Th concentrations exceed the concentrations predicted by the scavenging models in the absence of circulation, resulting in convex dissolved profiles (Francois, 2007). This is again clearly seen in measured seawater profiles (Rutgers van der Loeff and Berger, 1993) and model results (Fig. 7a). This trend is less apparent for ^{231}Pa (Fig. 7b) because of its slower response time, preventing the ^{231}Pa profiles from regaining linearity before reaching the Southern Ocean.

OSD
6, 2755–2829, 2009

4 Fractionation factors: data-model comparison

Fractionation factors (F) are most often obtained by measuring dissolved and particulate ^{231}Pa and ^{230}Th concentrations in the same seawater sample and applying Eq. (4) (e.g. Walter et al., 1997; Moran et al., 2002). These measured values are generally viewed as being mostly controlled by particle composition, with opal having a much lower F than the other major constituents of marine particles (Chase et al., 2002; Guo et al., 2002; Geibert and Usbeck, 2004). Our model reflects the generally accepted view that F is much lower in the opal dominated Southern Ocean than in the carbonate-dominated Atlantic Ocean and we chose adsorption and desorption rate constants to generate "equilibrium" fractionation factor broadly consistent with field observations (Table 3). The fractionation factor generated by the model using Eq. (4) indicates, however, that F is also significantly affected by the sinking rate of particles and ocean circulation (Fig. 8). This is because the chemical equilibrium between particles and seawater cannot be reached when particles sink through vertical dissolved ^{230}Th and ^{231}Pa concentration gradients. In the absence of circulation, we can rearrange Eqs. (4–6) to show that:

$$F = \frac{K_1^{\mathrm{Th}}(S + K_{-1}^{\mathrm{Pa}}Z)}{K_1^{\mathrm{Pa}}(S + K_{-1}^{\mathrm{Th}}Z)} \tag{10}$$

If the two nuclides have identical desorption rate constants, F would be independent of sinking rates in the absence of circulation. However, if $K_{-1}^{\mathrm{Pa}} < K_{-1}^{\mathrm{Th}}$ and $K_1^{\mathrm{Pa}} < K_1^{\mathrm{Th}}$ (Table 1) then F calculated with sinking particles rises well above equilibrium values and gradually decreases towards the equilibrium value with depth (Fig. 8a). When particles sink through the Atlantic Meridional Overturning cell, the fractionation factors estimated from Eq. (4) drop below the equilibrium fractionation factor within the core of the NADW (Fig. 8b). The fractionation factors measured in the field are therefore not directly comparable to those derived from equilibrium absorption experiments conducted in the laboratory (e.g. Geibert and Usbeck, 2004; Guo et al., 2002).

In contrast to the F generated by our model, the fractionation factors measured by Moran et al. (2002) and Scholten et al. (2008) in the equatorial and southern Atlantic increase with depth down to ~1500m and stay roughly constant or decrease further down. Also, the natural variability in F is much larger than the range observed in our model. The reason for this discrepancy could be depth variation in particle composition, a factor that is not taken into account in our model. Scholten et al. (2008) invoke a drop in the opal content of particles to explain the trend. However, the few available data on the composition of suspended particles (in the Sargasso Sea, Sherrell and Boyle, 1992; and in the North Pacific, Sherrell et al. 1998) do not show a clear trend with depth (except for one profile taken in spring 1991 in the North Pacific). Clearly, more data are needed before adding this variable in any model and this discrepancy must be left unresolved for now.

5 ^{230}Th and ^{231}Pa distribution in the control run

Since our control run is broadly consistent with the limited water column data that are available, we can discuss the general distribution of ^{230}Th and ^{231}Pa generated by the model with some level of confidence.

5.1 Dissolved ^{230}Th

The model clearly generates the downward penetration of low dissolved ^{230}Th by deep convection in the high northern Atlantic (Fig. 9a). The horizontal isolines between 20° N and 30° S indicate however that the vertical dissolved ^{230}Th profiles quickly regain linearity, as is observed in the field data. South of 30° S, dissolved ^{230}Th concentrations start to increase at all depths as a result of deep water upwelling (Fig. 2). The increase in dissolved ^{230}Th concentration is enhanced south of 50° S by the lower adsorption rate constants imposed in this region to reflect the dominance of biogenic silica (Table 1), while the formation of AABW results in dissolved ^{230}Th maxima at intermediate

OSD
6, 2755–2829, 2009

depths, similar to observations (Fig. 7a). In surface water, dissolved ^{230}Th concentration is significantly higher in the southern ocean, as has been noted in field data (Rutgers van der Loeff and Berger, 1993; Walter et al., 2001; Chase et al. 2003)

5.2 Particulate ^{230}Th

The pattern of distribution of particulate ^{230}Th concentration (Fig. 9b) is similar to that of dissolved ^{230}Th. There is a conspicuous maximum in particulate ^{230}Th just north of the southern opal belt, which is a result of the increase in dissolved ^{230}Th concentration resulting from deep water upwelling. The sharp drop in particulate ^{230}Th further south is a direct consequence of the lower K_1^{Th} in the southern ocean. Total ^{230}Th concentration profiles measured in the western (Table 2, Fig. 10) and eastern (Scholten et al., 2008) South Atlantic display a near bottom maximum similar to that generated by the model. This result may help explain the presence of a near-bottom maximum in total ^{230}Th when there are no clear evidence for the presence of a nepheloid layer (Scholten et al., 2008). However, our model generates these near-bottom maxima further south than observed, suggesting that a better representation of the AMOC in our model may require that the shoaling of the deep limb of the overturning cell starts further to the north.

The fraction of total ^{230}Th in particulate form generated by the model ($[^{230}\mathrm{Th}]_p/[^{230}\mathrm{Th}]_t$) ranges from 0.18 to 0.22 at low latitude (Fig. 9c), which is also conforming to field observations (Bacon and Anderson, 1982; Moran et al., 2002). In the Southern Ocean below 1000 m, the model produces somewhat lower fractions in particulate form (0.16–0.18), reflecting the lower affinity of biogenic silica for Th (Table 1). Somewhat higher fractions are generated in the upper water column of the Southern Ocean (0.22) and in the Nordic Sea (0.28) reflecting deep convection and higher residence time of particles in these waters.

OSD
6, 2755–2829, 2009

5.3 Dissolved ^{231}Pa

As for dissolved ^{230}Th, the model produces a clear downward penetration of low dissolved ^{231}Pa by deep convection at high northern latitudes (Fig. 9d). However, following expectations and observations, the minimum associated with the core of the NADW propagates much further south, reaching the southern ocean. South of 30° S, dissolved ^{231}Pa concentrations start to increase as a result of deep water upwelling but the effect is not as pronounced as for ^{230}Th because of the higher adsorption rate constants imposed in the southern ocean to reflect the dominance of biogenic silica (Table 1). Surface water dissolved ^{231}Pa concentrations are significantly higher in the southern ocean, but the effect is less pronounced than for ^{230}Th because of the higher scavenging rate of ^{231}Pa.

5.4 Particulate ^{231}Pa

The most prominent feature in the distribution of particulate ^{231}Pa concentration is the concentration maximum in the southern ocean (Fig. 9e), resulting from the higher K_1^{Pa} used in this region. The fraction of particulate ^{231}Pa generated by the model north of 45° S remains uniform between 0.04 and 0.05 (Fig. 9f), in general agreement with observations (Moran et al., 2002), while the higher values generated in the southern ocean (0.16–0.20) are consistent with some of the extreme values reported by Rutgers van der Loeff and Berger (1993). Profiles of total ^{231}Pa generated in the south Atlantic in the model are intermediate between measurements made in the western and eastern side of the basin (Fig. 11). The lower concentrations measured in the western Atlantic suggest that the Western Boundary Undercurrent rather than boundary scavenging plays a major role in controlling the distribution of ^{231}Pa in the water column of this region.

OSD
6, 2755–2829, 2009

5.5 Dissolved $^{231}Pa/^{230}Th$

Modeled dissolved $^{231}Pa/^{230}Th$ ratios systematically decrease with water depth in the North and Equatorial Atlantic, while this trend is less pronounced in the South Atlantic (Fig. 9g). Data from nine of the North and equatorial Atlantic stations presented in Table 2 reflect this trend with a clear decrease in dissolved $^{231}Pa/^{230}Th$ with depth below 500 m (Fig. 12). In shallower water, dissolved $^{231}Pa/^{230}Th$ is more variable. This may be a result of the short residence times of ^{230}Th and ^{231}Pa at these shallow depths and their limited lateral transport. Shallow dissolved $^{231}Pa/^{230}Th$ are likely to be more affected by local changes in particle composition. The lack of a clear trend with depth below 1000 m generated by the model in the South Atlantic is consistent with the observations of Scholten et al. (2008).

The model also predicts that the highest ratios would be found in the surface water of the South Atlantic (Fig. 9g). Walter et al. (2001) report an increasing trend in surface water dissolved $^{231}Pa/^{230}Th$ from 0.5 to 2.0 between 65° S and 40° S (their Fig. 4c). However, water column profiles from the South Atlantic available to date (Moran et al., 2002) fail to document the predicted large ratios in surface water. High ratios are generated in our model because surface waters from the southern ocean with relatively high dissolved ^{230}Th and ^{231}Pa concentrations are advected north. Since ^{230}Th is more quickly removed by scavenging, dissolved $^{231}Pa/^{230}Th$ initially increases to eventually decrease farther north as the scavenging of ^{231}Pa "catches up" with that of ^{230}Th. Evidently, the complexity of surface water movement in the South Atlantic cannot be fully captured in our simple 2-D model and these very high surface values may be artifacts of our simplified circulation. This question needs to be further explored with three dimensional models.

5.6 Particulate $^{231}Pa/^{230}Th$

The distribution of particulate $^{231}Pa/^{230}Th$ generated by the model is shown in Fig. 9h. We can take these values as representing the $^{231}Pa/^{230}Th$ that sediments would have

OSD
6, 2755–2829, 2009

if they were deposited at a given depth and latitude. However, as mentioned when discussing the fractionation factors, settling particles in our model are not in chemical equilibrium with surrounding waters. When particles reach the seafloor, they could possibly come into equilibrium with bottom waters. Whether they do or not depends on how long they are in contact with bottom waters before burial as a result of sedimentation and bioturbation. With the rate constants used in our model, it would take 1–3 years (depending on initial conditions) for surface sediments to be within 95% of their equilibrium value with bottom waters. We can calculate sediment ^{231}Pa/^{230}Th at equilibrium with bottom waters using $[X]_p/[X]_d = K_1^X/K_{-1}^X$ for ^{230}Th and ^{231}Pa (Fig. 9i). Partial equilibration would result in sediment ^{231}Pa/^{230}Th intermediate between values reported in Fig. 9h and i. The difference is relatively small in deep water but significantly larger in shallower waters. This is consistent with the observation of Scholten et al. (2008) who remarked that, at shallow depths, ^{231}Pa/^{230}Th in suspended particles are significantly lower than ^{231}Pa/^{230}Th in surface sediments (their Fig. 5) and suggest that surface sediments do reach equilibrium with bottom water.

6 Sediment ^{231}Pa/^{230}Th: data-model comparison

In this section, we compare the distribution of sediment ^{231}Pa/^{230}Th generated by the model with ^{231}Pa/^{230}Th measured in Atlantic sediments as a test for further validation.

The distribution of particulate (Fig. 9h) and sediment (Fig. 9i) ^{231}Pa/^{230}Th generated by the model is clearly controlled both by circulation and particle composition. We find the lowest values near the base of the two overturning cells just downstream of the sites of deep water formation and the highest values in the Southern Ocean. The low values are clearly generated by the overturning circulation cells, while the high values in the southern ocean are a direct consequence of the particle composition.

Sediment ^{231}Pa/^{230}Th generally decreases with depth, a pattern dictated by trends in dissolved ^{231}Pa/^{230}Th which is generated by the overturning circulation. A similar decreasing trend from ~0.13 at ~1000m to ~0.04 at ~5000m has been reported by

OSD
6, 2755–2829, 2009

Scholten et al (2008) for surface sediments in the South Atlantic. Holocene ^{231}Pa/^{230}Th from the five North Atlantic cores discussed by Gherardi et al. (2009) also show a similar trend, with values approaching the production rate ratios for the two shallower cores and lower values for the three deeper cores (Table 4). Values reported for core tops from the Nordic Seas range from 0.07 to 0.09 (Yu et al., 1996). Our model generates these values with an equilibrum fractionation factor of 7.8, somewhat higher that the fractionation factors measured in the Labrador Sea (3–7; Moran et al., 2002). Significantly higher sediment ^{231}Pa/^{230}Th have been reported, however, just south of Iceland and the Denmark Strait (0.10–0.15; Yu et al., 1996; R. F. Anderson, personal communication, 2009) but they are generally found in sediments deposited between 1500 and 2000 m water depth and seems confined to a relatively small area where Leinen et al. (1986) report opal concentration (carbonate-free wt %) of up to 20%. With the fractionation factors reported in Table 3 and Fig. 8, our model generates sediment ^{231}Pa/^{230}Th below the production rate ratio at this depth range just south of the site of deep water formation (Fig. 9i). The model generates the high values reported in this region only if we lower the equilibrium fractionation factor to 3.9 (Fig. 13).

7 Discussion

7.1 The effect of AMOC on sediment ^{231}Pa/^{230}Th

In the absence of any circulation, the model generates a field of constant sediment ^{231}Pa/^{230}Th equal to the production rate ratio (0.092). In this case, changes in the fractionation factor (Table 3) produce changes in the dissolved ^{230}Th and ^{231}Pa fields but not in the particulate fields. The distribution of particulate and sediment ^{231}Pa/^{230}Th reported in Fig. 9h, i should thus provide information on the ocean overturning circulation. The model results clearly indicate, however, that the relationship between sediment ^{231}Pa/^{230}Th at any given site and the overturning circulation is very complex. Sediment ^{231}Pa/^{230}Th depends not only on the rate of the overturning and particle

scavenging, but also on the detailed geometry of the overturning cell and the distance between the coring site and the site of deep water formation. Sediment ^{231}Pa/^{230}Th reaches a minimum at a depth dictated by the geometry of the overturning cell and at latitude dictated by the position of the site of deep water formation and the strength of the overturning circulation (Fig. 14). Clearly, it is impossible to constrain the history of changes in the AMOC from the evolution of ^{231}Pa/^{230}Th at one site, as was attempted by McManus et al. (2004).

7.1.1 Vertical variations in sediment ^{231}Pa/^{230}Th induced by the AMOC

The use of sediment ^{231}Pa/^{230}Th to reconstruct past changes in the AMOC relies on the longer residence time of ^{231}Pa in the water column. While the short residence time of ^{230}Th severely limits the extent to which it can be laterally transported after its production by uranium decay, the longer residence time of ^{231}Pa results in its extensive redistribution by ocean circulation. The removal of the two radionuclides is controlled by reversible scavenging and without circulation their dissolved concentrations would increase linearly with depth (Bacon and Anderson, 1982). Consequently, the residence time of the two isotopes with respect to removal by scavenging also increases linearly with depth (residence time = seawater concentration / production rate). As a direct consequence, if the rate of lateral volume transport were the same at all depths, the fraction of the ^{231}Pa production that is laterally transported with the water would increase with depth. This effect contributes to the general decrease with depth in dissolved and particulate ^{231}Pa/^{230}Th generated by the model (Fig. 9g–i) and measured in sediments (Table 4). Very little ^{231}Pa can be laterally exported by circulation at shallow depths but an increasing fraction can be exported with increasing depth. Sediment ^{231}Pa/^{230}Th integrates the lateral export of ^{231}Pa over the entire overlying water column. The integration in terms of lateral volume transport, however, is not linear but weighed by the depth-dependent residence time of ^{231}Pa with respect to scavenging. At similar rates, shallow overturning cells lower sediment ^{231}Pa/^{230}Th at the base of the cells less than deeper overturning cells. The relationship between changes in sediment ^{231}Pa/^{230}Th

with depth and changes in lateral volume transport with depth is therefore complex and difficult to intuit. In our control run, sediment ^{231}Pa/^{230}Th reaches its lowest value at the depth where we find the highest rate of lateral volume transport (Fig. 14a and b), but, this is not always necessarily the case. For instance, if we use the zonally integrated overturning rates recently derived from the ECCO consortium dataset (Wunsch and Heimbach, 2006), the lowest sediment ^{231}Pa/^{230}Th is reached 1000 m below the depth of maximum lateral volume transport (Fig. 15a and b).

7.1.2 Horizontal variations in sediment ^{231}Pa/^{230}Th induced by the AMOC

Sediment ^{231}Pa/^{230}Th also changes systematically with latitude or distance from the site of deep water formation. Latitudinal changes in sediment ^{231}Pa/^{230}Th at the depth where the minimum ratio is reached documents a initial decrease with distance from the site of deep water formation, followed by an increase (Fig. 14c). Dissolved ^{230}Th and ^{231}Pa concentrations are low throughout the water column at the site of deep water formation (Fig. 4). Because of its shorter residence time, ^{230}Th concentration increases faster to reach its steady-state concentration with respect to scavenging (Eq. 9), thereby gradually decreasing dissolved, particulate and sediment ^{231}Pa/^{230}Th. Once dissolved ^{230}Th has reached its maximum value, the slower increase in dissolved ^{231}Pa results is a slow increase in ^{231}Pa/^{230}Th further downstream.

7.1.3 Changes in sediment ^{231}Pa/^{230}Th resulting from changes in the rate of the AMOC

Increasing the rate of overturning in the control run without changing the geometry of the overturning cell has several effects on the distribution of Atlantic sediment ^{231}Pa/^{230}Th: (1) it pushes the zone of minimum ^{231}Pa/^{230}Th farther away from the site of deep water formation (Fig. 14c); (2) the latitudinal minimum in sediment ^{231}Pa/^{230}Th does not decrease, but instead increases (Fig. 14b and c) (3) sediment ^{231}Pa/^{230}Th also increases at the site of deep water formation and directly south of it (Fig. 14c); (4)

the vertical gradient of sediment ^{231}Pa/^{230}Th at the latitude corresponding to the minimum sediment ^{231}Pa/^{230}Th increases (Fig. 14b); (5) the largest decrease in sediment ^{231}Pa/^{230}Th downstream of the deep water formation zone is found in the Southern and equatorial region (Fig. 14c). Even without changing the geometry of the overturning cell and particle scavenging, the same value of sediment ^{231}Pa/^{230}Th can be generated at one site by different rates of overturning. For instance, the same value of 0.052 is produced at latitude 36.25° N at 3635 m with overturning rates of 10.25 Sv and 30.75 Sv (Fig. 14c). This observation reinforces the fact that sediment ^{231}Pa/^{230}Th at one site cannot constrain uniquely the rate of the AMOC.

7.1.4 Changes in sediment ^{231}Pa/^{230}Th resulting from changes in the geometry of the AMOC

We find systematic changes in the distribution of sediment ^{231}Pa/^{230}Th when we impose a shallower overturning cell without changing the rate of overturning: (1) the depth of minimum sediment ^{231}Pa/^{230}Th tends to shoal (Fig. 15a and b), although that might not be always the case; (2) the latitudinal gradient at the depth of minimum sediment ^{231}Pa/^{230}Th decreases (higher sediment ^{231}Pa/^{230}Th in the North Atlantic and lower sediment ^{231}Pa/^{230}Th in the South Atlantic, Fig. 15c) because ^{231}Pa has a shorter residence time in shallower water and is less effectively exported horizontally; (3) sediment ^{231}Pa/^{230}Th increases rapidly with depth below the base of the overturning cell (Fig. 15b), largely corroborating the finding of Thomas et al. (2006) that the sediment ^{231}Pa/^{230}Th signal generated by a shallow overturning circulation is, if not totally absent, at least strongly attenuated in sediments deposited more than 1000 m below the base of the overturning cell.

OSD
6, 2755–2829, 2009

7.1.5 Possible sampling strategy to constrain past changes in AMOC from sediment $^{231}Pa/^{230}Th$

These results suggest a possible sampling strategy to constrain past changes in the rate and geometry of the AMOC. A series of bathymetric profiles down the eastern and western slope of the North Atlantic, the Mid Ocean Ridge, or the flanks of seamounts, with due attention to possible changes in sediment composition, could document the vertical and horizontal sediment $^{231}Pa/^{230}Th$ gradients and the depth of minimum sediment $^{231}Pa/^{230}Th$ for different time slices. The shape of the vertical profiles would inform us on the geometry of the meridional overturning cells, while the gradients (horizontal and vertical) would provide constraints on the rate of the overturning. Figures 14 and 15 also suggest that sediment $^{231}Pa/^{230}Th$ at the site of deep water formation may be sensitive to the rate and depth of the AMOC. Whether these simple systematic trends can be reproduced in more complex circulation models, however, still needs to be verified.

7.2 The effect of AABW on sediment $^{231}Pa/^{230}Th$

Figure 9i clearly indicates that the overturning cell initiated in the Southern Ocean by the formation of AABW significantly contributes to lowering sediment $^{231}Pa/^{230}Th$ in the South Atlantic. If we eliminate the formation of AABW, sediment $^{231}Pa/^{230}Th$ in the South Atlantic significantly increases (Fig. 16). The process whereby AABW is producing these low sediment $^{231}Pa/^{230}Th$ is the same as for the northern overturning cell but the effect is found at greater depth and is less pronounced because of the smaller flow of water involved and the higher initial dissolved ^{230}Th and ^{231}Pa in the water that generates AABW. The low sediment $^{231}Pa/^{230}Th$ (<0.05) in the deep Southeast Atlantic (Scholten et al., 2008) are consistent with the importance of AABW in generating low $^{231}Pa/^{230}Th$ in the South Atlantic and suggest that sedimentary records in this region, if unaffected by changes in opal flux, could generate important constraints on variations in the rate of formation of this important water mass.

OSD
6, 2755–2829, 2009

7.3 The effect of particle composition on sediment $^{231}Pa/^{230}Th$

As already indicated above, in the presence of circulation and/or mixing, localized changes in particle composition and fractionation factors produce dramatic but localized changes in sediment $^{231}Pa/^{230}Th$ (Fig. 13). Such changes can be taken into account by analyzing the opal content of the sediment from which the $^{231}Pa/^{230}Th$ record is obtained (Gherardi et al., 2009) with, however, one important caveat. Opal is undersaturated throughout the ocean and much of it dissolves before burial. Below a certain threshold in opal flux and sediment mass accumulation rates, opal is not preserved in sediments but the $^{231}Pa/^{230}Th$ generated by the presence of opal in sinking particles could persist. We could further address this question by using a diagenetic model (e.g. Khalil et al., 2007) to estimate the opal concentration in sinking particles reaching the seafloor from sediment mass accumulation rates and use this information to estimate the range of possible fractionation factors to be applied at this site using the sediment trap data compilation of Chase et al. (2003). However, distinguishing between the importance of changes in circulation and opal flux will eventually be best addressed by generating a database large enough to obtain a near-synoptic view of the spatial distribution of sediment $^{231}Pa/^{230}Th$ for each time slice of interest, since the distribution generated by the overturning circulation is clearly distinct from the distribution generated by the distribution of opal productivity in the ocean.

While Fig. 13 clearly demonstrates the potential impact of localized variations in fractionation factors, it also shows, and maybe more importantly, that such changes in the North Atlantic have little impact on the $^{231}Pa/^{230}Th$ deposited downstream ($\Delta^{231}Pa/^{230}Th<0.002$; Fig. 13b). This is however not the case when we change the fractionation factor in the Southern Ocean (Fig. 17). Doubling the equilibrium fractionation factor in the Southern ocean from 0.9 to 1.8 not only decreases sediment $^{231}Pa/^{230}Th$ in the Southern Ocean from ~0.3 to ~0.2 but also uniformly increases sediment $^{231}Pa/^{230}Th$ along the latitudinal transect of the Atlantic by nearly ~0.01. Reducing the fractionation factor increases the Southern Ocean ^{231}Pa sink and has the

OSD
6, 2755–2829, 2009

opposite effect. However, the slope of the latitudinal gradient of sediment ^{231}Pa/^{230}Th in the Atlantic is not significantly affected and could still be used to constrain the rate of the overturning. Nonetheless, accurately assessing the extent of the southern ocean ^{231}Pa sink will be important to evaluate the rate of AMOC.

8 Conclusions

We have developed a simple 2-D circulation-scavenging model to address some of the questions that have been raised concerning the use of sediment ^{231}Pa/^{230}Th as a paleocirculation tracer (Keigwin and Boyle, 2008; Scholten et al., 2008; Lippold et al., 2009). Although our circulation model is clearly too simple to capture all the complexity of ocean circulation, it reproduces many of the features observed in the distribution of dissolved ^{230}Th and ^{231}Pa and sediment ^{231}Pa/^{230}Th and provides a tool to start assessing the relative importance of circulation and particle scavenging in controlling the distribution pattern of sediment ^{231}Pa/^{230}Th in the Atlantic.

The circulation scheme imposed in our model broadly reflects the flow of the main deep Atlantic water masses (NADW, AABW). The detailed geometry of the two overturning cells and the parameters of the imbedded scavenging model have been tuned to reproduce the broad features of the distribution of dissolved ^{230}Th and ^{231}Pa and fractionation factors measured in the water column to date. The model produces a general decrease in dissolved, particulate and sediment ^{231}Pa/^{230}Th with depth, which is consistent with field observations (Fig. 12; Scholten et al., 2008; Gherardi et al., 2009). It also produces patterns in the distribution of sediment ^{231}Pa/^{230}Th which could be used to distinguish the circulation signal from the effect of particle scavenging. The model output also suggests sampling strategies to optimize the information in past circulation that could be derived from sediment ^{231}Pa/^{230}Th. The most robust circulation signals generated by the model are the vertical and horizontal sediment ^{231}Pa/^{230}Th gradients, which changes systematically with the rate and geometry of the AMOC (Figs. 14 and 15). However, we still need to establish whether these diagnostic trends

OSD
6, 2755–2829, 2009

can also be produced with more complex 3-D circulation models.

We have used our 2-D model to test the extent to which changes in fractionation factor can obliterate the patterns of sediment ^{231}Pa/^{230}Th generated by the overturning circulation. While it is clear that changes in particle composition in the North Atlantic can change sediment ^{231}Pa/^{230}Th locally, our model indicates that the ^{231}Pa/^{230}Th pattern generated by circulation further downstream is not significantly affected. This may be different for the Southern Ocean, which is the main sink for ^{231}Pa in our model. Changing the fractionation factor in the Southern Ocean offsets ^{231}Pa/^{230}Th but has little impact on the gradients below 1500 m, and the information on the rate and geometry of the overturning circulation is still preserved.

Our 2-D model largely corroborates the results from the 1-D model of Thomas et al. (2006) and indicates that the sediment ^{231}Pa/^{230}Th signal is rapidly attenuated in sediment deposited below the base of the overturning cell. Finally, low sediment ^{231}Pa/^{230}Th in the South Atlantic (Scholten et al., 2008) appears to be due to the formation of AABW, which suggest that the ^{231}Pa/^{230}Th sedimentary record in this region, just north of the zone influenced by biogenic silica, could be used to constrain past changes in the rate of formation of this water mass.

Acknowledgements. R. Francois acknowledges financial support from the CFCAS, NSERC and NSF. Sea water analyses were conducted with the help of A. Fleer and S. Brown-Leger (WHOI), and M. Soon (UBC).

References

Bacon, M. P.: Tracers of chemical scavenging in the ocean – boundary effects and large-scale chemical fractionation, Philos. T. Roy. Soc. A, 325, 147–160, 1988.

Bacon, M. P. and Anderson, R. F.: Distribution of thorium isotopes between dissolved and particulate forms in the deep sea, J. Geophys. Res., 87, 2045–2056, 1982.

Bacon, M. P., Huh, C. A., Fleer, A. P., and Deuser, W. G.: Seasonality in the flux of natural radionuclides and plutonium in the deep Sargasso Sea, Deep-Sea Res. A, 32, 273–286, 1985.

Boyle, E. A. and Keigwin, L.: North-Atlantic thermohaline circulation during the past 20000 years linked to high-latitude surface-temperature, Nature, 330, 35–40, 1987.
Chase, Z., Anderson, R. F., Fleisher, M. Q., and Kubik, P. W.: The influence of particle composition and particle flux on scavenging of Th, Pa and Be in the ocean, Earth Planet. Sci. Lett., 204, 215–219, 2002.
Chase, Z., Anderson, R. F., Fleisher, M. Q., and Kubik, P. W.: Scavenging of ^{230}Th, ^{231}Pa and ^{10}Be in the Southern Ocean (SW Pacific sector): the importance of particle flux, particle composition and advection, Deep-Sea Res. II, 50, 739–768, 2003.
Clark, P. U., Pisias, N. G., Stocker, T. F., and Weaver, A. J.: The role of the thermohaline circulation in abrupt climate change, Nature, 415, 863–869, 2002.
Clegg, S. L. and Whitfield, M.: A generalized model for scavenging of trace metals in the open ocean, II. Thorium scavenging, Deep-Sea Res. A, 38, 91–120, 1991.
Clegg, S. L., Bacon, M. P., and Whitfield, M.: Application of a generalized scavenging model to thorium isotope and particle data at equatorial and high-latitude sites in the Pacific-Ocean, J. Geophys. Res.-Ocean., 96, 20655–20670, 1991.
Delanghe, D., Bard, E., and Hamelin, B.: New TIMS constraints on the uranium-238 and uranium-234 in seawaters from the main ocean basins and the Mediterranean Sea, Mar. Chem., 80, 79–93, 2002.
Francois, R.: Paleoflux and paleocirculation from sediment ^{230}Th and ^{231}Pa/^{230}Th, in: Proxies in Late Cenozoic Paleoceanography, edited by: Hillaire-Marcel, C. and de Vernal, A., Elsevier, 681–716, 2007.
Francois, R., Frank, M., van der Loeff, M. M. R., and Bacon, M. P.: Th-230 normalization: An essential tool for interpreting sedimentary fluxes during the late Quaternary, Paleoceanography, 19, PA1018, doi:10.1029/2003PA000939, 2004.
Friedrichs, M. A. and Hall, M. M.: Deep circulation in the tropical North Atlantic, J. Mar. Res., 51, 697–736, 1993.
Ganachaud, A. and Wunsch, C.: Improved estimates of global ocean circulation, heat transport and mixing from hydrographic data, Nature, 408, 453–457, 2000.
Geibert, W. and Usbeck, R.: Adsorption of thorium and protactinium onto different particle types: Experimental findings, Geochim. Cosmochim. Acta, 68, 1489–1501, 2004.
Gherardi, J.-M., Labeyrie, L., Francois, R., McManus, J. F., Skinner, L. C., and Cortijo, E.: Evidence from the Northeastern Atlantic basin for variability in the rate of the meridional overturning circulation through the last deglaciation, Earth Planet. Sci. Lett., 240, 710–723,

2005.
Gherardi, J.-M., Labeyrie, L., Nave, S., Francois, R., McManus, J. F., and Cortijo, E.: Glacial-interglacial circulation changes inferred from $^{231}Pa/^{230}Th$ sedimentary record in the North Atlantic region, Paleoceanography, 24, PA2204, doi:10.1029/2008PA001696, 2009.
Guo, L. D., Chen, M., and Gueguen, C.: Control of Pa/Th ratio by particulate chemical composition in the ocean, Geophys. Res. Lett., 29, 1961, doi:10.1029/2002GL015666, 2002.
Hall, I. R., Moran, S. B., Zahn, R., Knutz, P. C., Shen, C.-C., and Edwards, R. L.: Accelerated drawdown of meridional overturning in the late-glacial Atlantic triggered by transient pre-H event freshwater perturbation, Geophys. Res. Lett., 33, L16616, doi:10.1029/2006GL026239, 2006.
Keigwin, L. D. and Boyle, E. A.: Did North Atlantic overturning halt 17 000 years ago? Paleoceanography, 23, L16616, doi:10.1029/2007PA001500, 2008.
Khalil, K., Rabouille, C., Gallinari, M., Soetaert, K., DeMaster, D. J., and Ragueneau, O.: Constraining biogenic silica dissolution in marine sediments: A comparison between diagenetic models and experimental dissolution rates, Mar. Chem., 106, 223–238, 2007.
Krishnaswami, S., Sarin, M. M., and Somayajulu, B. L. K.: Chemical and radiochemical investigation of surface and deep particles of the Indian Ocean, Earth Planet. Sci. Lett., 54, 81–96, 1981.
Legrand, P. and Wunsch, C.: Constraints from paleotracer data on the North-Atlantic circulation during the Last Glacial Maximum, Paleoceanography, 10, 1011–1045, 1995.
Leinen, M., Cwienk, D., Heath, G. R., Biscaye, P. E., Kolla, V., Thiede, J., and Dauphin J. P.: Distribution of biogenic silica and quartz in recent deep-sea sediments, Geology, 14, 199–203, 1986.
Lippold, J., Gruetzner, J., Winter, D., Lahaye, Y., Mangini, A., and Christl, M.: Does sedimentary Pa-231/Th-230 from the Bermuda Rise monitor past Atlantic Meridional Overturning Circulation? Geophys. Res. Lett., 36, PA1101, doi:10.1029/2009GL038068, 2009.
Lynch-Stieglitz, J., Adkins, J. F., Curry, W. B., Dokken, T., Hall, I. R., Herguera J. C., Hirschi, J. J.-M., Ivanova, E. V., Kissel, C., Marchal, O., Marchitto, T. M., McCave, I. N., McManus, J. F., Mulitza, S., Ninnemann, U., Peeters, F., Yu, E.-F., and Zahn, R.: Atlantic meridional overturning circulation during the Last Glacial Maximum, Science, 316, 66–69, 2007.
Macdonald, A. M.: The global ocean circulation: a hydrographic estimate and regional analysis, Prog. Oceanogr., 41, 281–382, 1998.
Marchal, O., Francois, R., Stocker, T. F., and Joos, F.: Ocean thermohaline circulation and

sedimentary Pa-231/Th-230 ratio, Paleoceanography, 15, 625–641, 2000.
McManus, J. F., Francois, R., Gherardi, J.-M., Keigwin, L., and Brown-Leger, S.: Collapse and rapid resumption of Atlantic Meridional Circulation linked to deglacial climate changes, Nature 428, 834–837, 2004.
Moran, S. B., Charette, M. A., Hoff, J. A., Edwards, R. L., and Landing, W. M.: Distribution of ^{230}Th in the Labrador Sea and its relation to ventilation, Earth Planet. Sci. Lett., 150, 151–160, 1997.
Moran, S. B., Hoff, J. A., Buesseler, K. O., and Edwards, R. L.: High-Precision Th-230 and Th-232 In The Norwegian Sea and Denmark by Thermal Ionization Mass-Spectrometry, Geophys. Res. Lett., 22, 2589–2592, 1995.
Moran, S. B., Shen, C. C., Edmonds, H. N., Weinstein, S. E., Smith, J. N., and Edwards R. L.: Dissolved and particulate Pa-231 and Th-230 in the Atlantic Ocean: constraints on intermediate/deep water age, boundary scavenging, and Pa-231/Th-230 fractionation, Earth Planet. Sci. Lett., 203, 999–1014, 2002.
Moran, S. B., Shen, C.-C., Weinstein, S. E., Hettinger, L. H., Hoff, J. H., Edmonds H. N., and Edwards, R. L.: Constraints on the deep water age and particle flux in the Equatorial and South Atlantic Ocean based on seawater ^{231}Pa and ^{230}Th data, Geophys. Res. Lett., 28, 2440–3437, 2001.
Nozaki, Y., Yang, H.-S., and Yamada, M.: Scavenging of thorium in the ocean, J. Geophys. Res., 92, 772–778, 1987.
Press, W. H., Teukolsky, S. A., Vetterling, W. T., and Flannery, B. P.: Numerical Recipies in C: The Art of Scientific Computing, 2nd edn, Cambridge University Press, 1992.
Robinson, L. F., Henderson, G. M., Hall, L., and Matthews, I.: Climatic control of riverine and Seawater uranium-isotope ratios, Science, 305, 851–854, 2004.
Rutgers Van Der Loeff, M. M. and Berger, G. W.: Scavenging of thorium-230 and protactinium-231 near the Antarctic polar front in the South Atlantic. Deep-Sea Res. I, 40, 339–357, 1993.
Schmittner, A., Yoshimori, M., and Weaver, A. J.: Instability of glacial climatea model of the ocean-atmosphere-cryosphere system, Science, 295, 1489–1493, 2002.
Scholten, J. C., Fietzke, J., Mangini, A., Garbe-Schonberg, C.-D., Eisenhauer, A., Schneider, R., and Stoffers, P.: Advection and scavenging: Effects on Th-230 and Pa-231 distribution off Southwest Africa, Earth Planet. Sci. Lett., 271, 159–169, 2008.
Scholten, J. C., Rutgers Van Der Loeff, M. M. R., and Michel, A.: Distribution of Th-230 and Pa-231 in the water column in relation to the ventilation of the deep Arctic basins, Deep-Sea

Res. II, 42, 1519–1531, 1995.
Sherrell, R. M. and Boyle, E. A.: The trace-metal composition of suspended particles in the oceanic water column near bermuda, Earth Planet. Sci. Lett., 111, 155–174, 1992.
Sherrell, R. M., Field, M. P., and Gao, Y.: Temporal variability of suspended mass and composition in the Northeast Pacific water column: relationships to sinking flux and lateral advection, Deep-Sea Res. II, 45, 733–761, 1998.
Sloyan, B. M. and Rintoul, S. R.: The Southern Ocean Limb of the global deep overturning circulation, J. Phys. Oceanogr., 31, 143–173, 2001.
Talley, L. D., Reid, J. L., and Robbins, P. E.: Data-based meridional overturning streamfunctions for the global ocean, J. Climate, 16, 3213–3226, 2003.
Thomas, A. L., Henderson, G. M., and Robinson, L. F.: Interpretation of the ^{231}Pa/^{230}Th paleocirculation proxy: New water-column measurements from the southwest Indian Ocean, Earth Planet. Sci. Lett., 241, 493–504, 2006.
Walter, H. J., Geibert, W., Rutgers van der Loeff, M. M., Fischer, G., and Bathmann, U.: Shallow vs. deep-water scavenging of ^{231}Pa and ^{230}Th in radionuclide enriched waters of the Atlantic sector of the Southern Ocean, Deep-Sea Res. I, 48, 471–493, 2001.
Walter, H.-J., Van der Loeff, M. M. R., and Hoeltzen, H.: Enhanced scavenging of ^{231}Pa relative to ^{230}Th in the South Atlantic south of the Polar Front. Implications for the use of the ^{231}Pa/^{230}Th ratio as a paleoproductivity proxy, Earth Planet. Sci. Lett., 149, 85–100, 1997.
Yu, E. F., Francois, R., and Bacon, M. P.: Similar rates of modern and last-glacial ocean thermohaline circulation inferred from radiochemical data, Nature, 379, 689–694, 1996.

Table 1. List of abbreviations and values for the model parameters.

Variables	Symbol	Control run	Units
^{231}Pa production rate	P_{Pa}	0.00246	dpm/(m^{3}yr)
^{230}Th production rate	P_{Th}	0.0267	dpm/(m^{3}yr)
Particle sinking rate	S	500	m/yr
^{230}Th adsorption rate (70° N–50° S)			
0–250 m	K_1^{Th}	1.0	1/yr
250–500 m	K_1^{Th}	0.75	1/yr
>500m	K_1^{Th}	0.5	1/yr
^{230}Th adsorption rate (50° S-70° S)			
0–250 m	K_1^{Th}	0.6	1/yr
250–500 m	K_1^{Th}	0.45	1/yr
>500m	K_1^{Th}	0.3	1/yr
^{230}Th desorption rate (70° N-70° S)			
All depths	K_{-1}^{Th}	1.6	1/yr
^{231}Pa adsorption rate (70° N-42.5° S)			
0–250 m	K_1^{Pa}	0.08	1/yr
250–500 m	K_1^{Pa}	0.06	1/yr
>500m	K_1^{Pa}	0.04	1/yr
^{231}Pa adsorption rate (42.5°-45° S)			
0–250 m	K_1^{Pa}	0.2	1/yr
250–500 m	K_1^{Pa}	0.15	1/yr
>500m	K_1^{Pa}	0.1	1/yr
^{231}Pa adsorption rate (45°-47.5° S)			
0–250 m	K_1^{Pa}	0.3	1/yr
250–500 m	K_1^{Pa}	0.225	1/yr
>500m	K_1^{Pa}	0.15	1/yr
^{231}Pa adsorption rate (47.5° S-70° S)			
0–250 m	K_1^{Pa}	0.44	1/yr
250–500 m	K_1^{Pa}	0.33	1/yr
>500m	K_1^{Pa}	0.22	1/yr
^{231}Pa desorption rate (70° N-70° S)			
All depths	K_{-1}^{Pa}	1	1/yr

OSD
6, 2755–2829, 2009

Table 2. ^{230}Th and ^{231}Pa activities in seawater (dpm/1000kg).

W-A: Station EN407-3 (39°28′ N; 68°22′ W)		
Depth m	Diss. ^{230}Th dpm/1000kg (±95% CI)	Diss. ^{231}Pa
250	–	0.062±0.004
500	0.140±0.005	0.110±0.005
751	0.187±0.007	0.147±0.006
1001	0.204±0.008	0.134±0.006
1250	0.161±0.006	0.092±0.005
1501	0.265±0.009	0.148±0.009
1800	0.299±0.008	0.166±0.007
2200	0.338±0.011	0.176±0.007
2500	0.353±0.011	0.181±0.007
2750	0.329±0.019	0.165±0.011
2980	0.295±0.009	0.140±0.005

OSD
6, 2755–2829, 2009

Table 2. Continued.

W-B: Station EN407-4 (38°36′ N; 68°53′ W)		
Depth m	Diss. ^{230}Th dpm/1000kg (±95% CI)	Diss. ^{231}Pa
50	0.044±0.002	0.030±0.004
200	0.090±0.004	0.064±0.005
400	0.116±0.005	0.113±0.007
600	0.238±0.008	0.168±0.009
800	0.235±0.009	0.177±0.006
1000	0.242±0.009	0.152±0.008
1200	0.206±0.008	0.140±0.006
1400	0.247±0.008	0.147±0.006
1600	0.280±0.012	0.170±0.005
1800	0.299±0.010	0.155±0.006
2000	0.303±0.011	0.156±0.007
2200	0.340±0.011	0.193±0.008
2400	0.335±0.014	0.187±0.009
2600	0.337±0.014	0.182±0.007
2800	0.321±0.016	0.165±0.007
3000	0.344±0.015	0.156±0.006
3200	0.276±0.011	0.144±0.007
3400	0.227±0.013	0.125±0.005
3470	0.196±0.010	0.129±0.006

Table 2. Continued.

W-C: Station KNR07-4 (01°34′ N; 23°38′ W)		
Depth m	Diss. ^{230}Th dpm/1000kg (±95% CI)	Diss. ^{231}Pa
50	0.054±0.003	0.038±0.007
400	0.130±0.003	0.122±0.009
800	0.218±0.004	0.253±0.017
1100	0.284±0.005	0.310±0.021
1500	0.372±0.008	0.314±0.013
1800	0.430±0.009	0.290±0.011
2100	0.461±0.007	0.326±0.031
2400	0.489±0.007	0.323±0.019
2700	0.490±0.007	0.348±0.020
3000	0.477±0.007	0.314±0.015
3400	0.502±0.006	0.304±0.017
3800	0.571±0.008	0.264±0.015

OSD
6, 2755–2829, 2009

Table 2. Continued.

W-D: Station KNR07-3 (01°12′ S; 25°29′ W)		
Depth m	Diss. ^{230}Th dpm/1000kg (±95% CI)	Diss. ^{231}Pa
50	0.063±0.003	0.051±0.004
400	0.140±0.006	0.128±0.009
800	0.223±0.005	0.234±0.014
1000	0.274±0.004	0.292±0.012
1300	0.325±0.007	0.291±0.016
1500	0.377±0.008	0.275±0.013
2000	0.446±0.009	0.268±0.017
2500	0.449±0.006	0.300±0.016
3000	0.425±0.006	0.283±0.012
3500	0.470±0.006	0.236±0.012
4000	0.572±0.014	0.214±0.012
4500	0.800±0.009	0.263±0.013

OSD
6, 2755–2829, 2009

Table 2. Continued.

W-E: Station KNR07-2 (03°44′ S; 27°58′ W)		
Depth m	Diss. ^{230}Th dpm/1000kg (±95% CI)	Diss. ^{231}Pa
50	0.051±0.003	0.052±0.011
300	0.174±0.006	0.104±0.010
900	0.271±0.007	0.271±0.012
1100	0.295±0.008	0.308±0.017
1600	0.431±0.010	0.292±0.017
2100	0.490±0.012	0.278±0.014
2600	0.532±0.011	0.321±0.015
3100	0.598±0.019	0.291±0.016
3600	0.594±0.011	0.227±0.014
4000	0.690±0.011	0.229±0.019
4400	0.848±0.015	0.266±0.014
5000	0.845±0.018	0.262±0.010

Table 2. Continued.

W-F: Station KNR07-1 (07°10′ S; 31°15′ W)		
Depth m	Diss. ^{230}Th dpm/1000kg (±95% CI)	Diss. ^{231}Pa dpm/1000kg (±95% CI)
50	0.062±0.003	0.036±0.006
450	0.172±0.008	0.200±0.016
900	0.304±0.010	0.330±0.018
1350	0.389±0.007	0.282±0.015
1756	0.485±0.009	0.306±0.020
2250	0.492±0.014	0.279±0.011
3150	0.567±0.017	0.278±0.013
3556	0.568±0.010	0.238±0.010
4000	0.734±0.011	0.262±0.012
4456	0.908±0.013	0.267±0.016
5000	0.813±0.013	0.254±0.012

Table 2. Continued.

E-A: Station EN328-9 (45°32′ N; 21°24′ W)		
Depth m	Diss. ^{230}Th dpm/1000kg (±95% CI)	Diss. ^{231}Pa
50	0.030±0.001	0.066±0.004
400	0.139±0.003	0.097±0.007
800	0.194±0.003	0.146±0.008
1000	0.230±0.004	0.168±0.008
1500	0.250±0.004	0.163±0.009
2000	0.312±0.005	0.169±0.010
2500	0.282±0.004	0.176±0.011
3000	0.244±0.009	0.198±0.012
3500	0.272±0.005	0.269±0.014
3827	0.332±0.005	0.300±0.014

OSD
6, 2755–2829, 2009

Table 2. Continued.

E-B: Station EN328-7 (31°00′ N; 31°02′ W)		
Depth m	Diss. ^{230}Th dpm/1000kg (±95% CI)	Diss. ^{231}Pa
50	0.058±0.002	0.069±0.007
400	0.151±0.003	0.078±0.005
800	0.193±0.004	0.147±0.006
1000	0.279±0.006	0.205±0.007
1500	0.361±0.007	0.237±0.011
2000	0.429±0.007	0.274±0.014
2500	0.504±0.008	0.283±0.012
3000	0.651±0.010	0.323±0.011
3500	0.795±0.014	0.364±0.014
4000	0.775±0.012	0.365±0.013
4375	0.767±0.017	0.343±0.010

OSD
6, 2755–2829, 2009

Table 2. Continued.

E-C: Station EN328-4 (22°00′ N; 36°31′ W)		
Depth m	Diss. ^{230}Th dpm/1000kg (±95% CI)	Diss. ^{231}Pa
50	0.062±0.002	0.058±0.005
400	0.174±0.003	0.096±0.006
800	0.231±0.004	0.190±0.008
1000	0.275±0.005	0.240±0.011
1300	0.401±0.007	0.289±0.011
1500	0.453±0.008	0.323±0.013
2000	0.689±0.013	0.414±0.012
2500	0.814±0.011	0.449±0.014
3000	0.902±0.012	0.423±0.013
4000	0.983±0.012	0.368±0.013
4997	0.900±0.009	0.292±0.014
5506	0.843±0.010	0.280±0.010

OSD
6, 2755–2829, 2009

Table 2. Continued.

E-D: Station KNR07-9 (12°56′ N; 23°21′ W)		
Depth m	Diss. ^{230}Th dpm/1000kg (±95% CI)	Diss. ^{231}Pa
50	0.061±0.003	0.067±0.011
450	0.142±0.004	0.126±0.017
900	0.233±0.005	–
1300	0.334±0.006	0.349±0.031
1700	0.461±0.008	0.429±0.030
2100	0.561±0.009	0.408±0.028
2500	0.545±0.008	0.415±0.027
3000	0.679±0.011	0.437±0.026
3500	0.770±0.009	0.446±0.038
4000	0.699±0.008	0.332±0.013
4500	0.657±0.012	0.260±0.013
4700	0.590±0.008	0.239±0.010

Table 2. Continued.

E-E: Station KNR07-6 (10°04′ N; 23°14′ W)		
Depth m	Diss. ^{230}Th dpm/1000kg (±95% CI)	Diss. ^{231}Pa
50	0.088±0.002	0.077±0.007
450	0.164±0.003	0.132±0.014
900	0.228±0.005	0.227±0.013
1300	0.350±0.008	0.324±0.026
1700	0.466±0.007	0.356±0.021
2100	0.541±0.008	0.352±0.031
2500	0.620±0.010	0.431±0.028
3000	–	0.384±0.027
3500	0.731±0.010	0.366±0.025
4000	0.660±0.009	0.302±0.016
4500	0.707±0.011	0.266±0.012
5000	–	0.240±0.015

OSD
6, 2755–2829, 2009

Table 2. Continued.

E-F: Station KNR07-5 (07°50′ N; 24°37′ W)		
Depth m	Diss. ^{230}Th dpm/1000kg (±95% CI)	Diss. ^{231}Pa
50	0.056±0.002	0.057±0.006
450	0.150±0.004	0.086±0.007
900	0.254±0.006	0.274±0.013
1300	0.369±0.008	0.310±0.020
1700	0.459±0.008	0.298±0.018
2100	0.554±0.010	0.390±0.020
2500	0.586±0.013	0.350±0.019
3000	0.671±0.013	0.358±0.019
3500	0.665±0.011	0.359±0.023
4000	0.640±0.010	0.300±0.023
4500	0.690±0.010	0.273±0.019
4700	0.702±0.015	0.248±0.017

Table 2. Continued.

Station KNR06-3 (29°32′ S; 43°20′ W)		
Depth m	Diss. ^{230}Th dpm/1000kg (±95% CI)	Diss. ^{231}Pa dpm/1000kg (±95% CI)
12	0.096±0.003	0.045±0.006
401	0.197±0.004	0.070±0.008
797	0.316±0.005	0.140±0.008
1202	0.494±0.006	0.260±0.012
1600	0.572±0.008	0.353±0.016
1998	–	0.307±0.015
2200	0.690±0.009	0.311±0.014
2400	0.692±0.009	0.344±0.020
2800	0.746±0.010	0.376±0.017
3197	–	0.308±0.012
3598	0.961±0.011	0.331±0.014
3944	1.412±0.014	0.326±0.015

OSD
6, 2755–2829, 2009

Table 3. "Equilibrium" Fractionation Factors.

Latitude	"Equilibrium Fractionation Factor"
70° N–42.5° S	7.8
42.5° S–45° S	3.1
45°–47.5° S	2.1
47.5° S–50° S	1.4
50° S–70° S	0.9

OSD
6, 2755–2829, 2009

Table 4. Holocene Pa/Th in 5 North Atlantic cores (Gherardi et al., 2009).

Core	Position	Water Depth (m)	Holocene $^{231}Pa/^{230}Th$
DAPC2	58°58′ N 09°36′ W	1709	0.093±0.001
MD95-2037	37°05′ N 32°01′ W	2150	0.093±0.004
SU81-18	37°46′ N 10°11′ W	3135	0.064±0.005
SU90-44	50°01′ N 17°06′ W	4279	0.052±0.004
OCE326-GGC5	33°42′ N 57°35′ W	4550	0.054±0.004

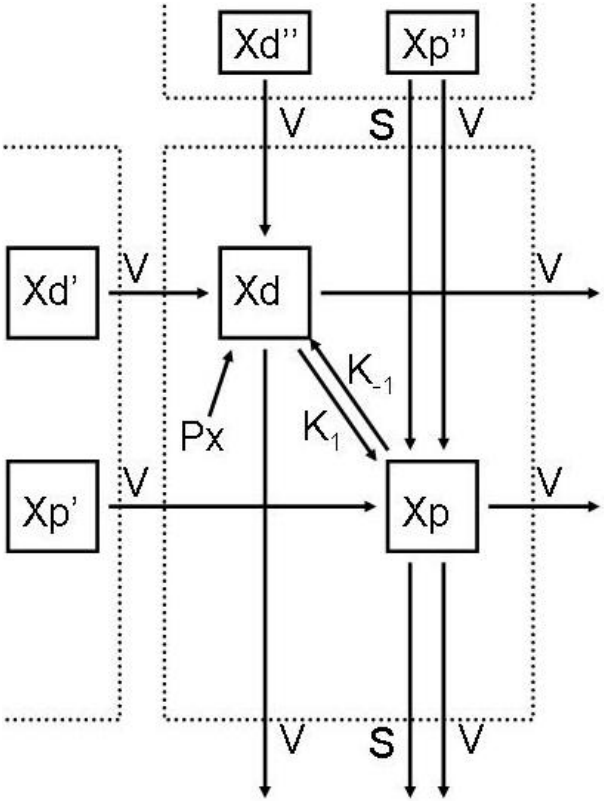

Fig. 1. The scavenging-circulation model consists of a meridional section (from 70° N to 70° S) evenly divided into 56×20 grids (20 layers evenly distributed over 5000 m depth and 56 columns evenly distributed over the meridional section; 2.5° latitude per column). In each box, X represents ^{230}Th or ^{231}Pa. Xd's=dissolved concentrations (dpmm^{-3}). Xp's=particulate concentrations (dpmm^{-3}). P_X=production rates from U decay (dpmm^{-3}y^{-1}). S=sinking rates of particles (my^{-1}). V=Transport rates (my^{-1}).

OSD
6, 2755–2829, 2009

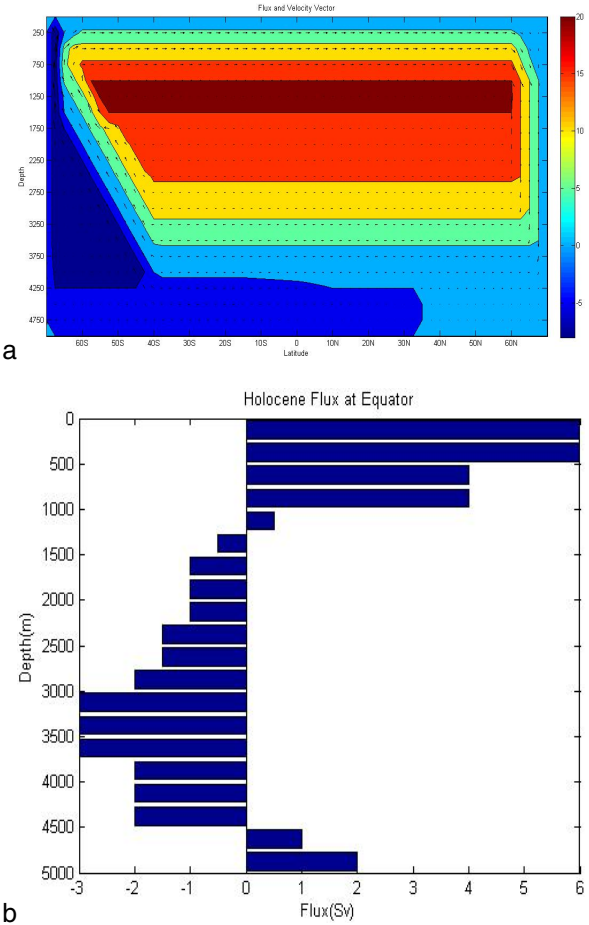

Fig. 2. (a) Velocity vector plot. Size of the arrows is proportional to the transport rates used in the model. **(b)** Overturning fluxes in the model at the equator.

OSD

6, 2755–2829, 2009

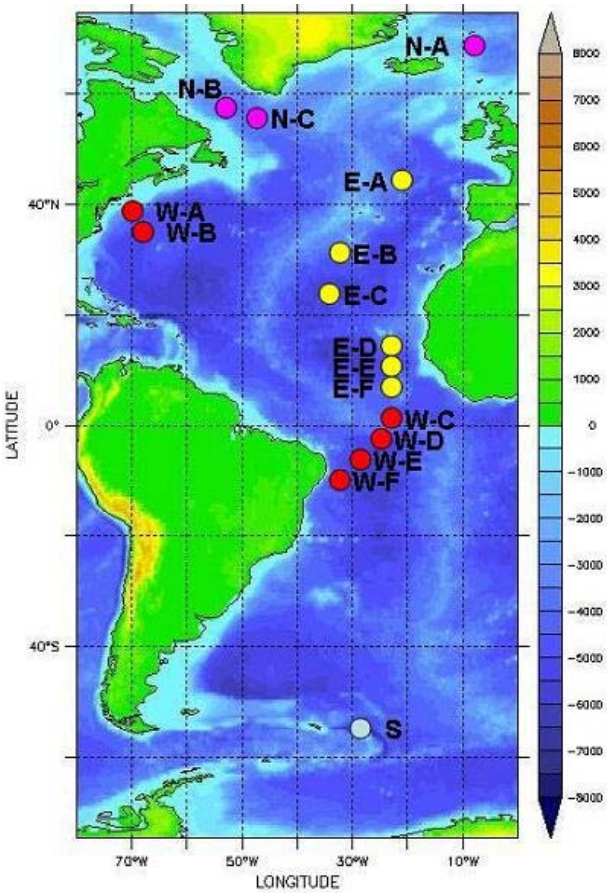

Fig. 3. Station locations for the water column profiles used to constrain the parameters in the model. Nordic Seas: N-A, N-B, N-C (Moran et al., 1995, 1997, 2002); Western Atlantic: W-A to W-F (Table 2); Eastern Atlantic: E-A to E-F (Table 2); Southern Ocean: S (Rutgers van der Loeff and Berger, 1993).

OSD

6, 2755–2829, 2009

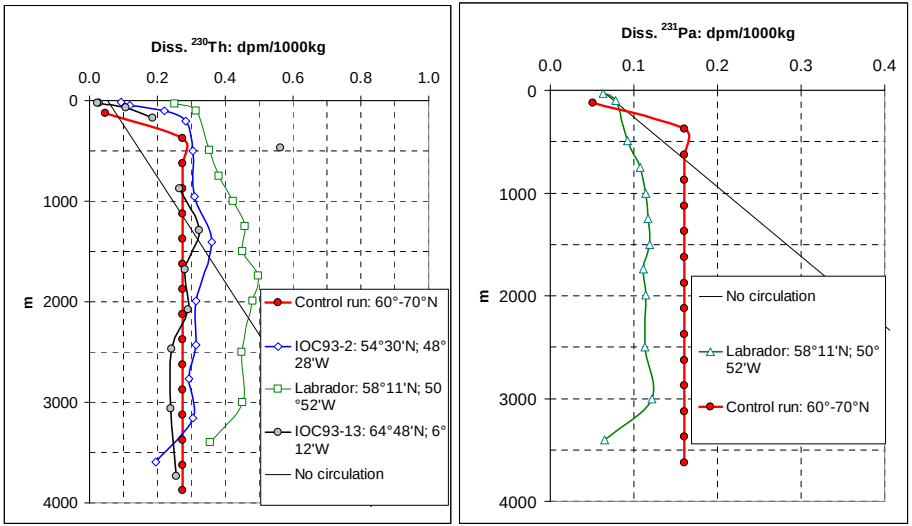

Fig. 4. Dissolved ^{230}Th and ^{231}Pa obtained with the control run at 60°–70° N and measured in the Norwegian Sea (IOC93-13: Moran et al., 1995) and the Labrador Sea in 1993 (IOC93-2; Moran et al., 1997) and 1999 (Labrador: Moran et al., 2002).

OSD

6, 2755–2829, 2009

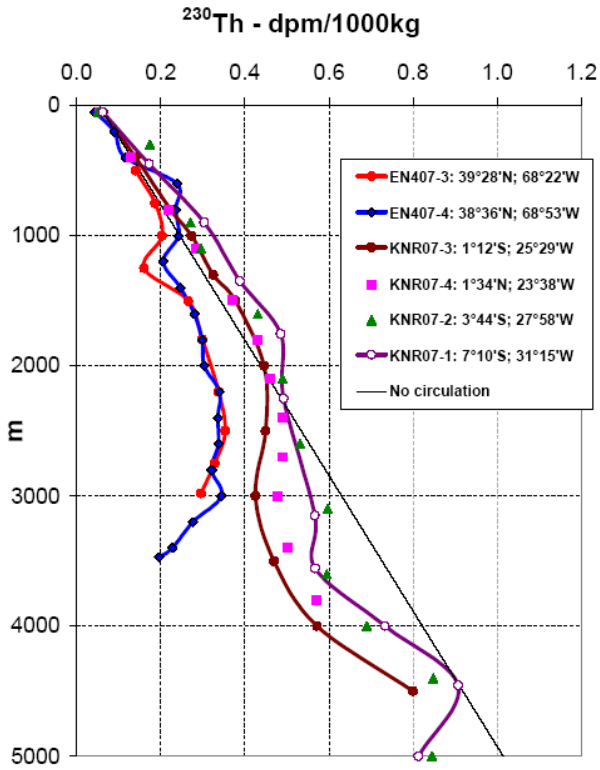

Fig. 5a. Dissolved ^{230}Th measured **(a)** in the western Atlantic, **(b)** in the eastern Atlantic, and **(c)** produced with the control run.

OSD

6, 2755–2829, 2009

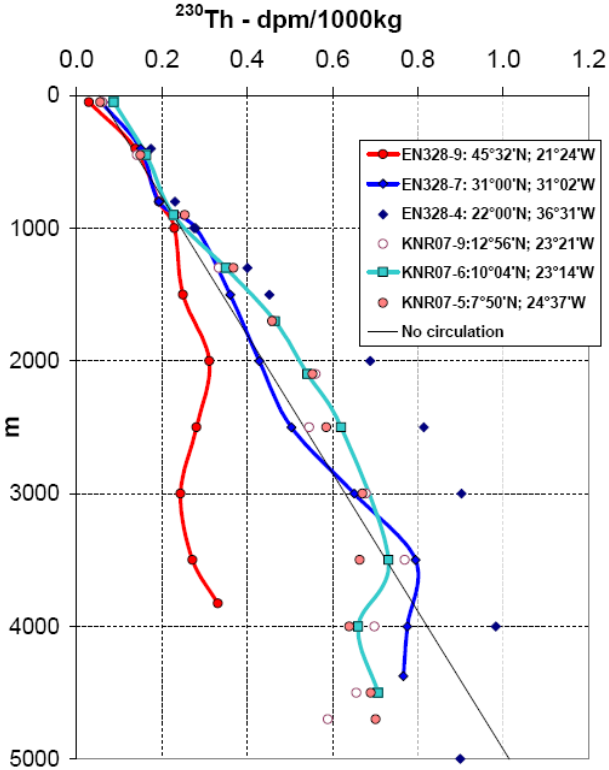

Fig. 5b. Continued.

OSD
6, 2755–2829, 2009

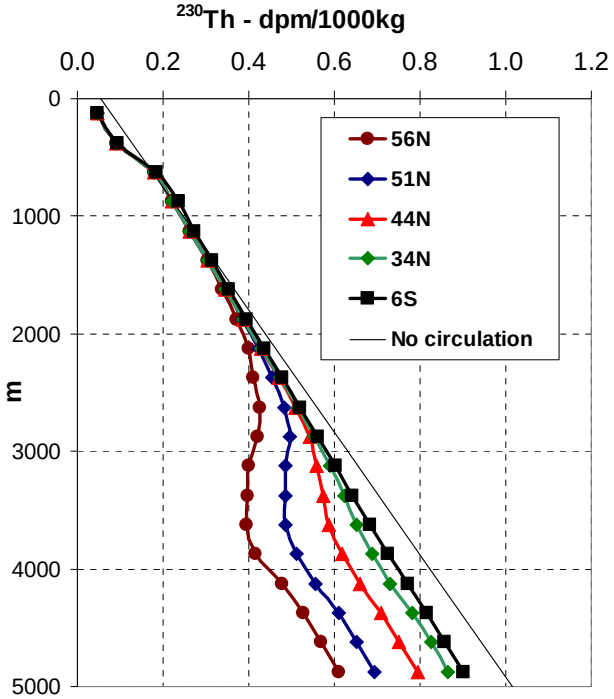

Fig. 5c. Continued.

OSD
6, 2755–2829, 2009

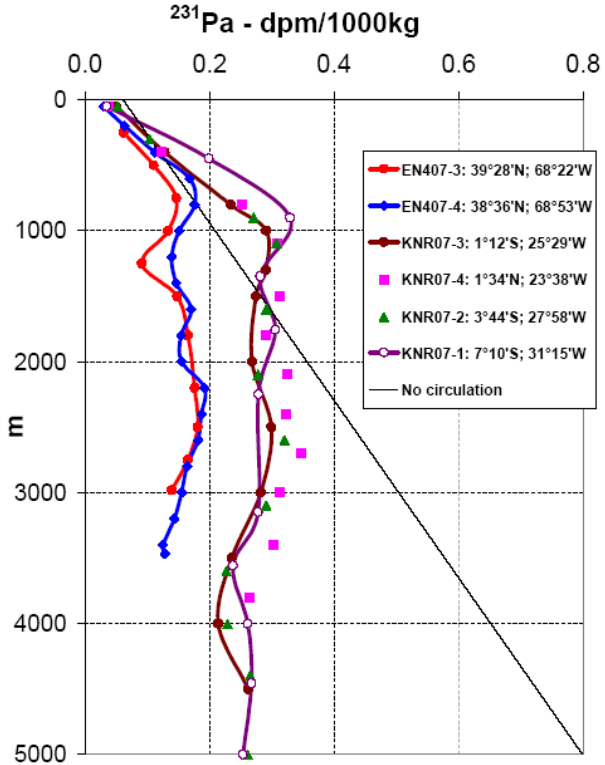

Fig. 6a. Dissolved ^{231}Pa measured **(a)** in the western Atlantic, **(b)** in the eastern Atlantic, and **(c)** produced with the control run.

OSD

6, 2755–2829, 2009

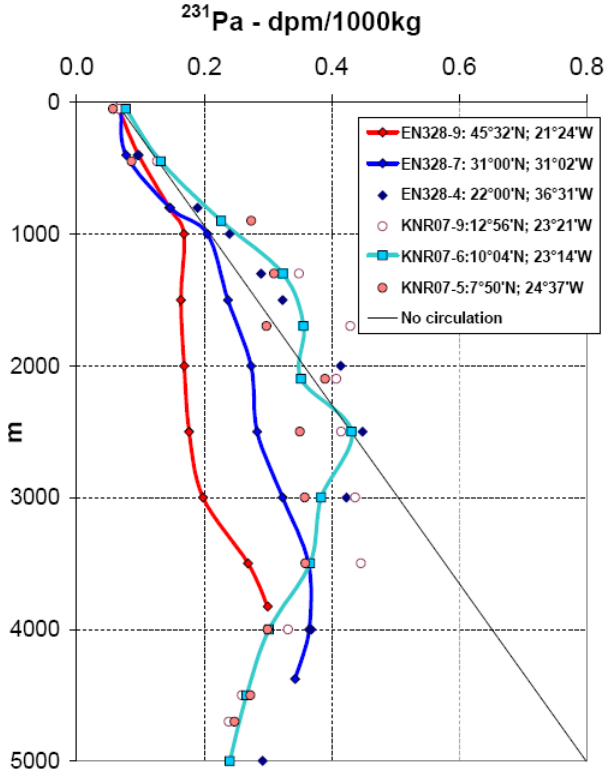

Fig. 6b. Continued.

OSD
6, 2755–2829, 2009

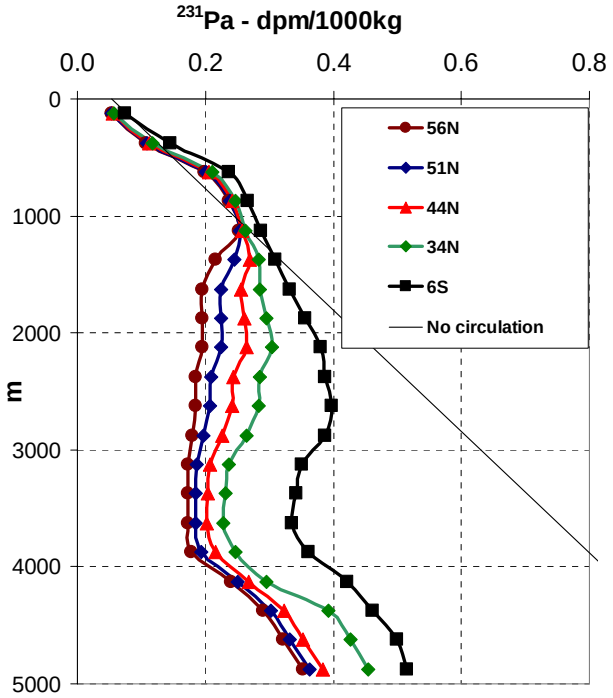

Fig. 6c. Continued.

OSD
6, 2755–2829, 2009

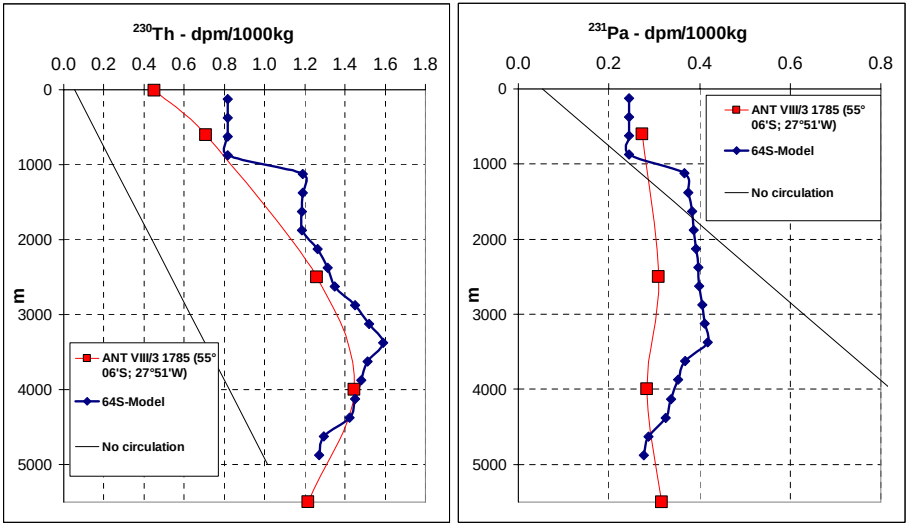

Fig. 7. Concentration profiles of dissolved ^{230}Th and ^{231}Pa measured (Rutgers van der Loeff and Berger, 1993) and modeled (control run) in the southern ocean.

OSD
6, 2755–2829, 2009

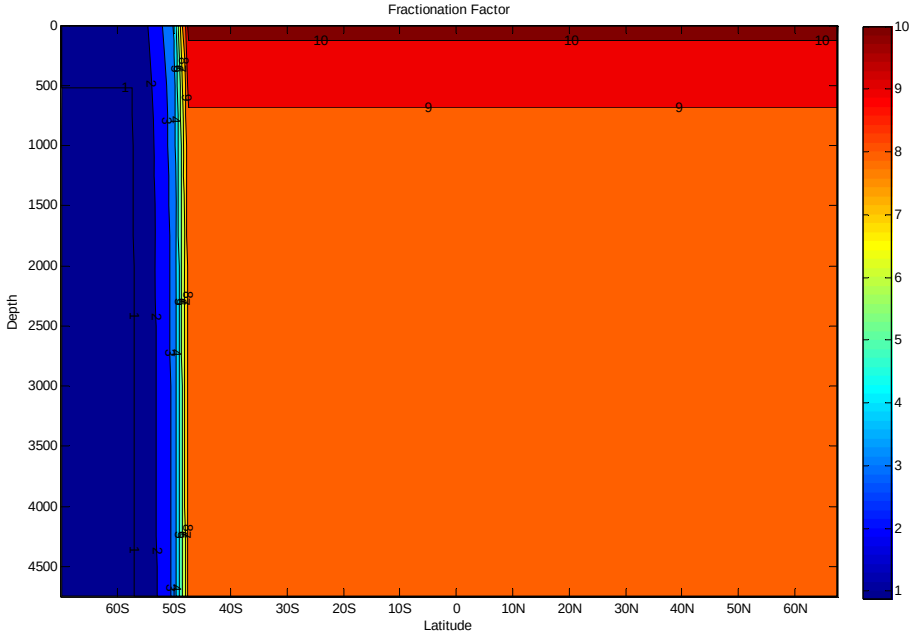

Fig. 8a. Distribution of fractionation factors: **(a)** obtained in our model with sinking particles but without circulation **(b)** obtained with sinking particles in the control run with AMOC (NADW: 21.5 Sv; AABW: 8 Sv). Note that sinking rates and circulation can significantly affect the fractionation factor defined as $(^{231}Pa_d/^{230}Th_d)/(^{231}Pa_p/^{230}Th_p)$ (see text for explanation).

OSD
6, 2755–2829, 2009

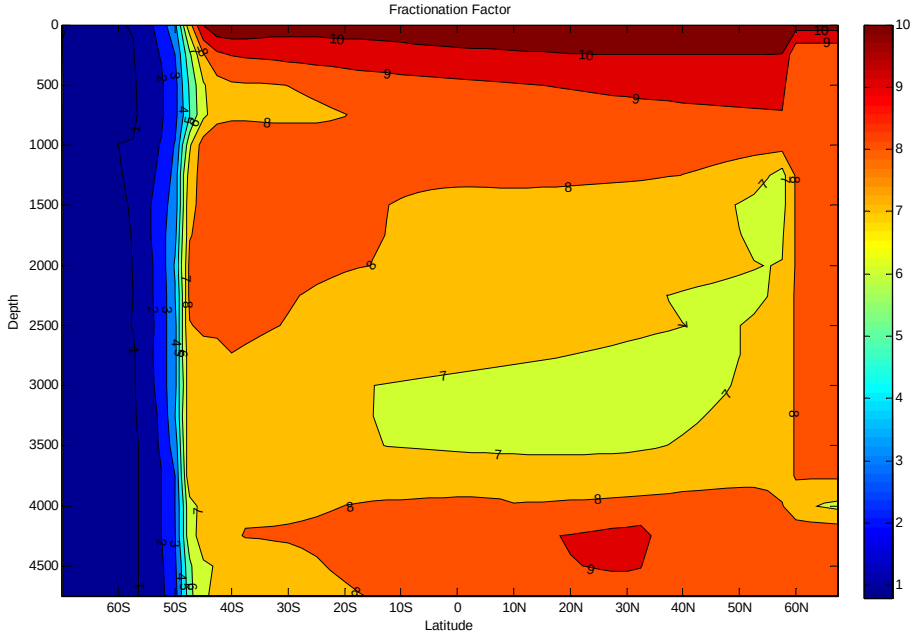

Fig. 8b. Continued.

OSD

6, 2755–2829, 2009

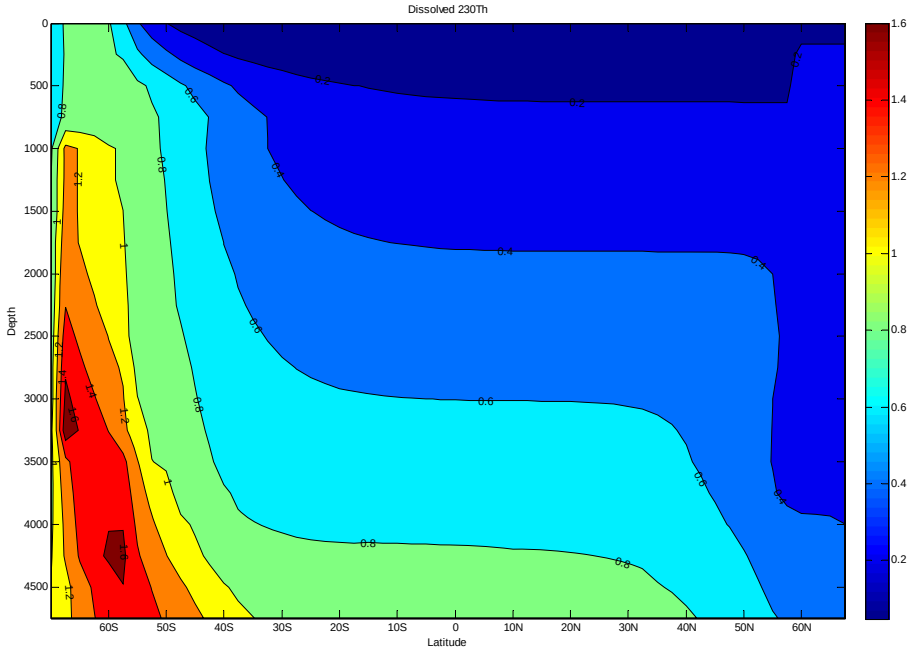

Fig. 9a. Dissolved ^{230}Th section generated by the model.

OSD

6, 2755–2829, 2009

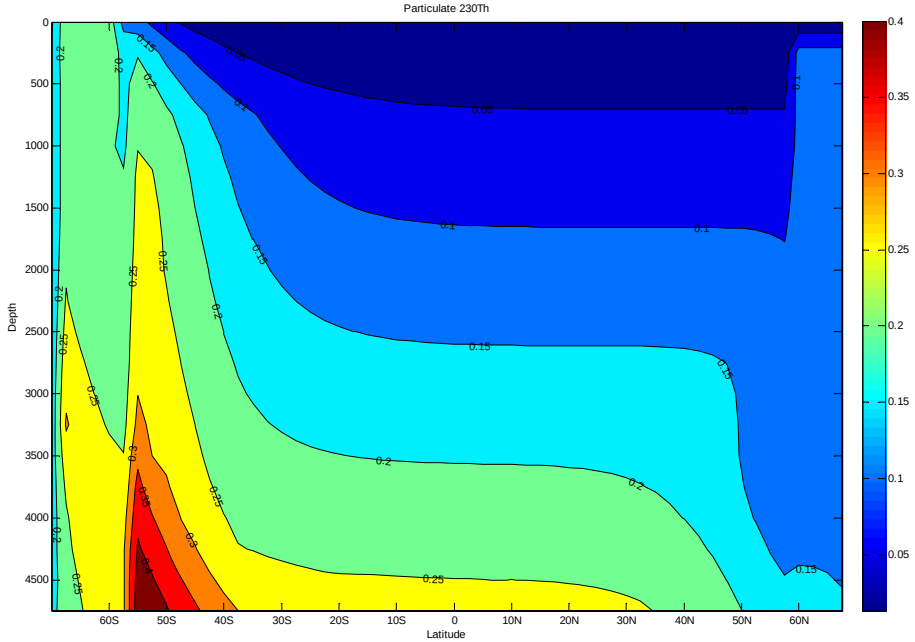

Fig. 9b. Particulate ^{230}Th section generated by the model.

OSD

6, 2755–2829, 2009

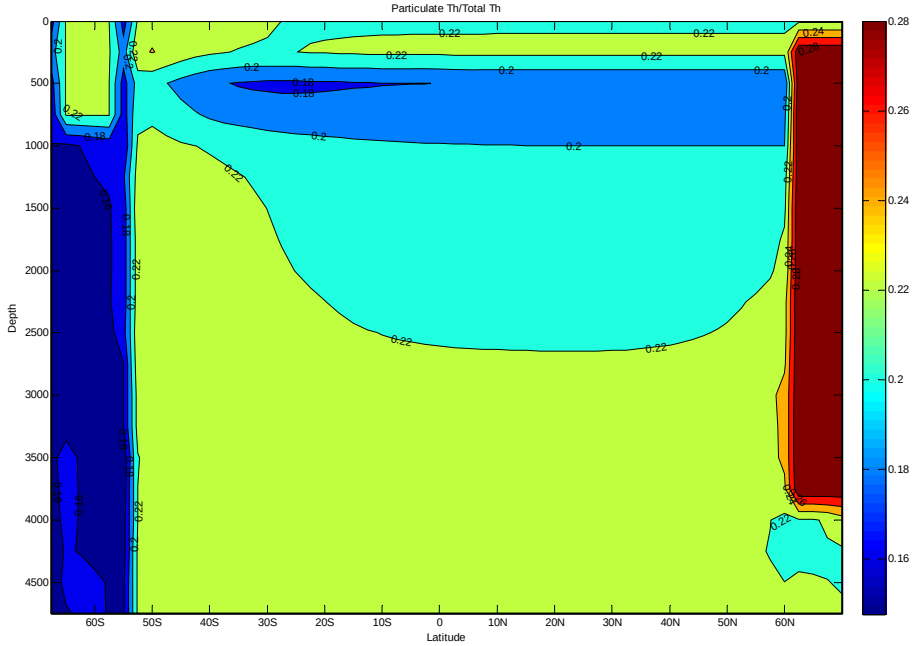

Fig. 9c. Fraction of total ^{230}Th associated with particles generated by the model.

OSD

6, 2755–2829, 2009

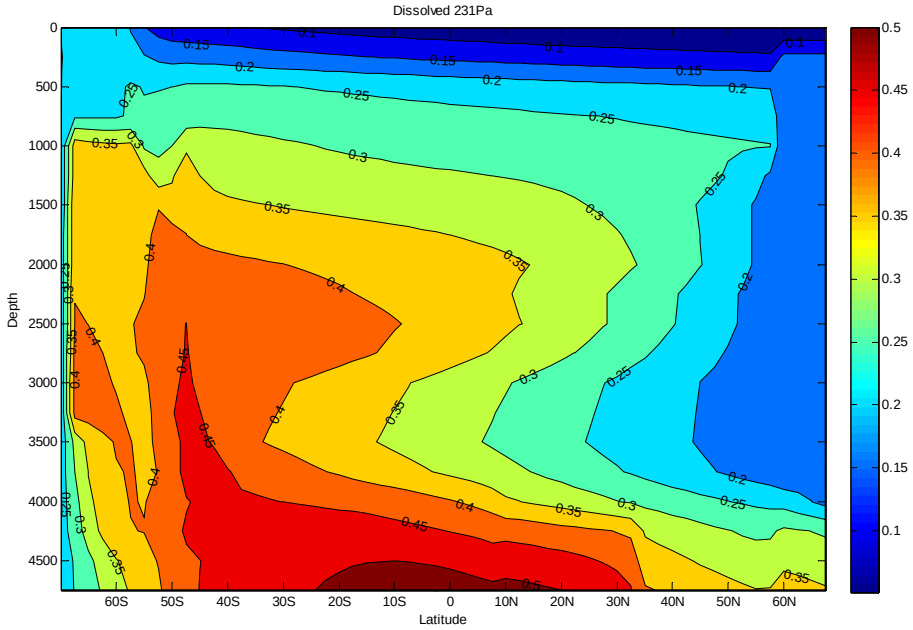

Fig. 9d. Dissolved ^{231}Pa section generated by the model.

OSD

6, 2755–2829, 2009

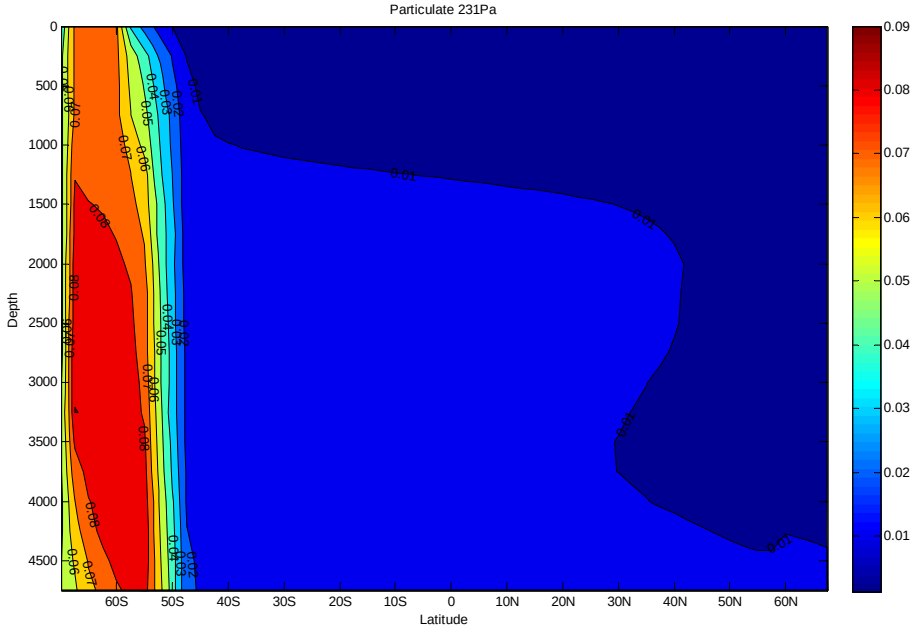

Fig. 9e. Particulate ^{231}Pa section generated by the model.

OSD

6, 2755–2829, 2009

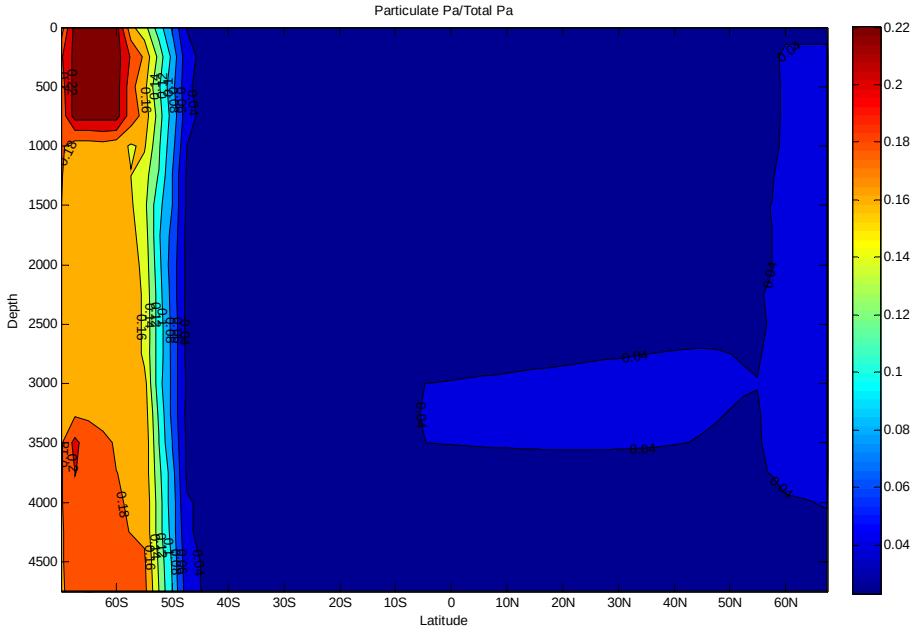

Fig. 9f. Fraction of total ^{231}Pa associated with particles generated by the model.

OSD
6, 2755–2829, 2009

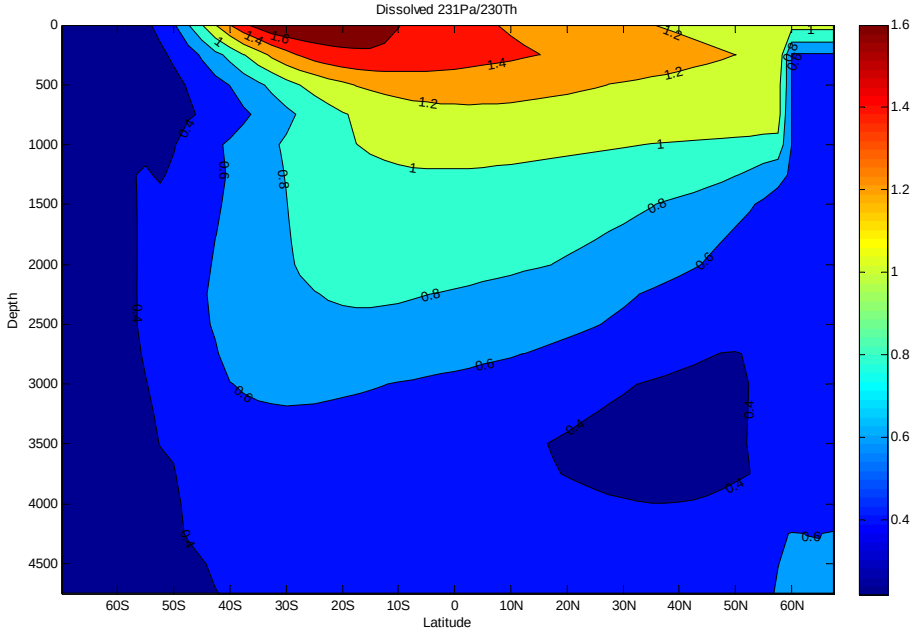

Fig. 9g. Dissolved ^{231}Pa/^{230}Th section generated by the model.

OSD

6, 2755–2829, 2009

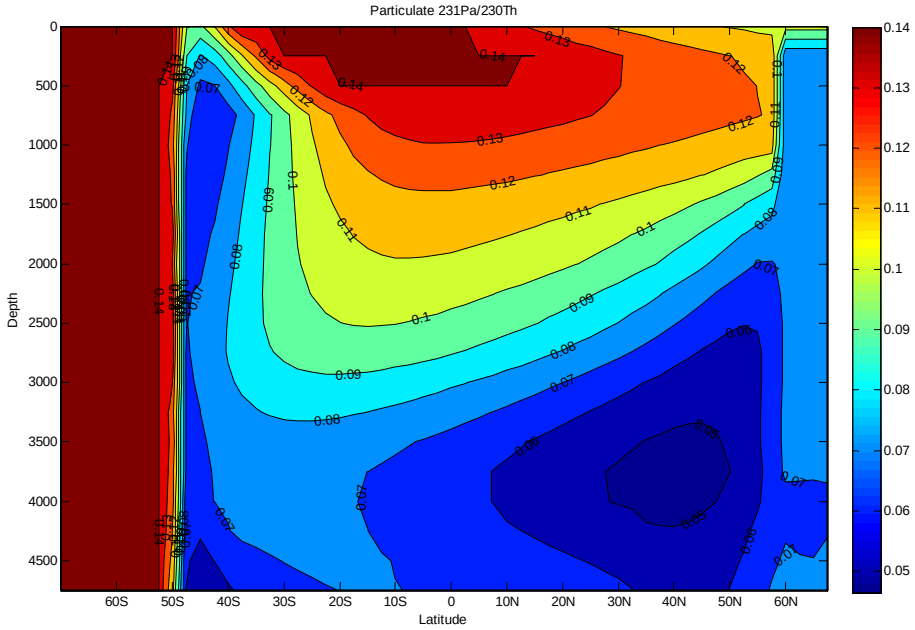

Fig. 9h. Particulate ^{231}Pa/^{230}Th section generated by the model.

OSD

6, 2755–2829, 2009

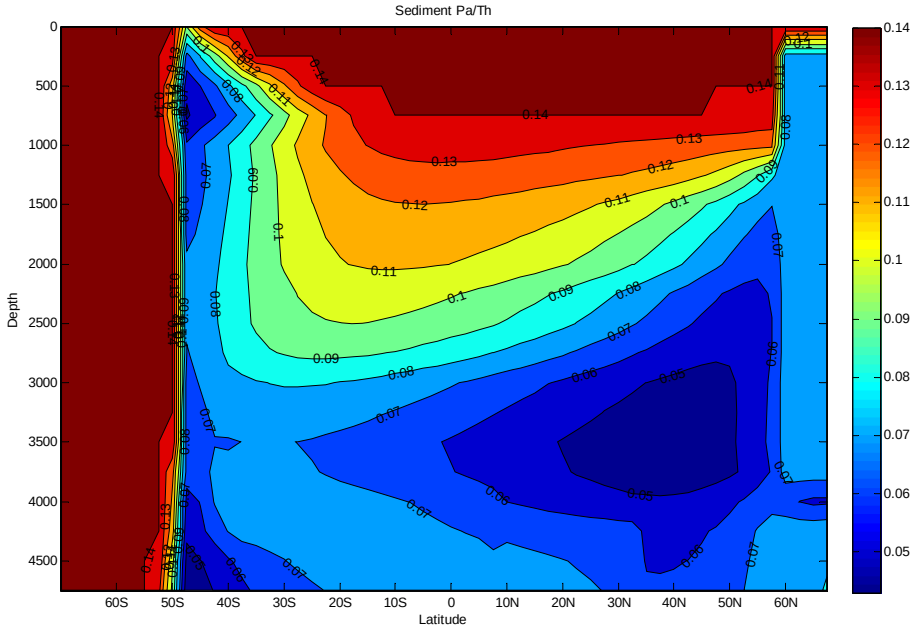

Fig. 9i. Sediment ^{231}Pa/^{230}Th section generated by the model assuming that sediment reach equilibrium with bottom water (see text for explanations).

OSD

6, 2755–2829, 2009

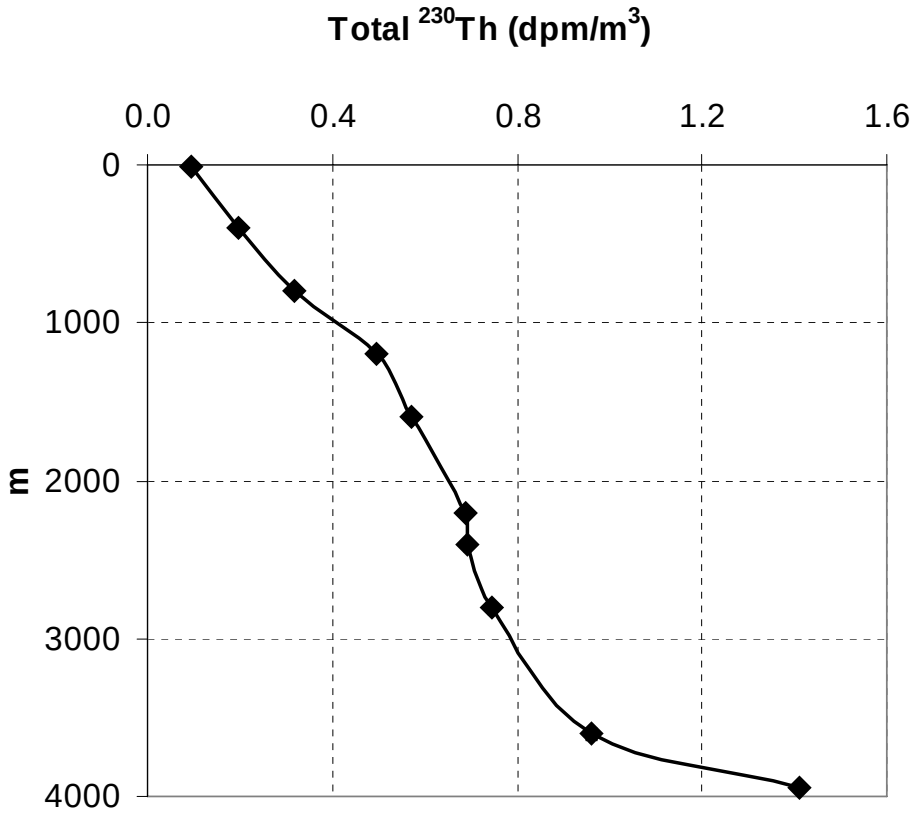

Fig. 10. Total ^{230}Th concentration measured in the Southwestern Atlantic at 29°32′ S; 43°20′ W (Station KNR06-3; Table 2) showing a near-bottom maximum similar to that generated in the South Atlantic by our model.

OSD
6, 2755–2829, 2009

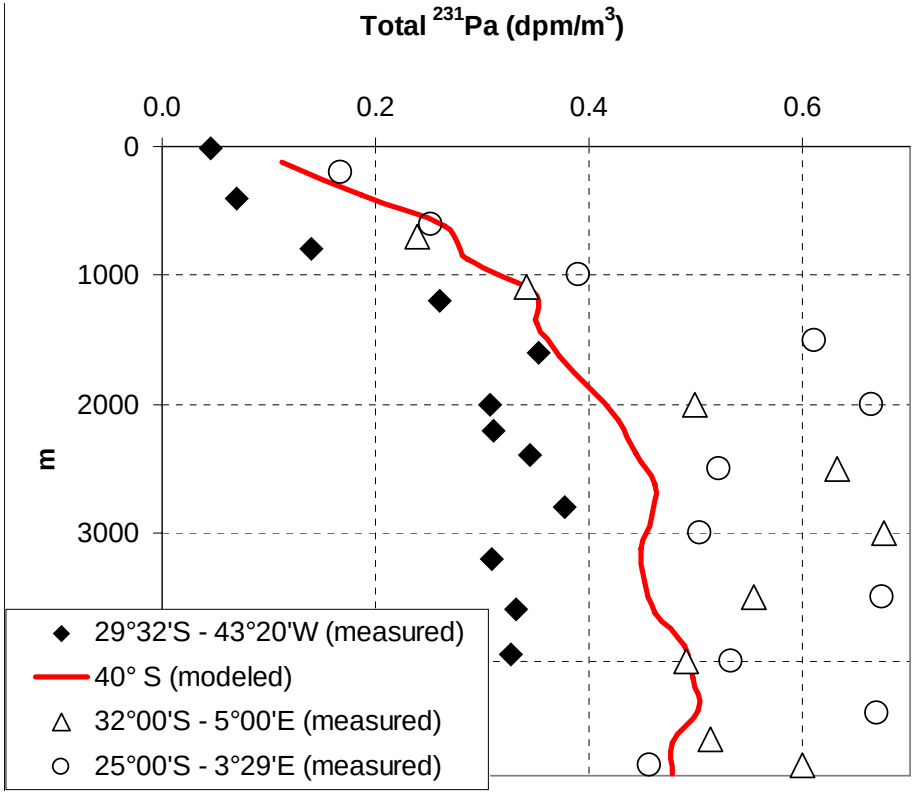

Fig. 11. Total ^{231}Pa concentration measured in the Southwestern Atlantic at 29°32′ S; 43°20′ W (Station KNR06-3; Table 2) and in the western South Atlantic (Scholten et al., 2008) compared to model results at 40° S.

OSD
6, 2755–2829, 2009

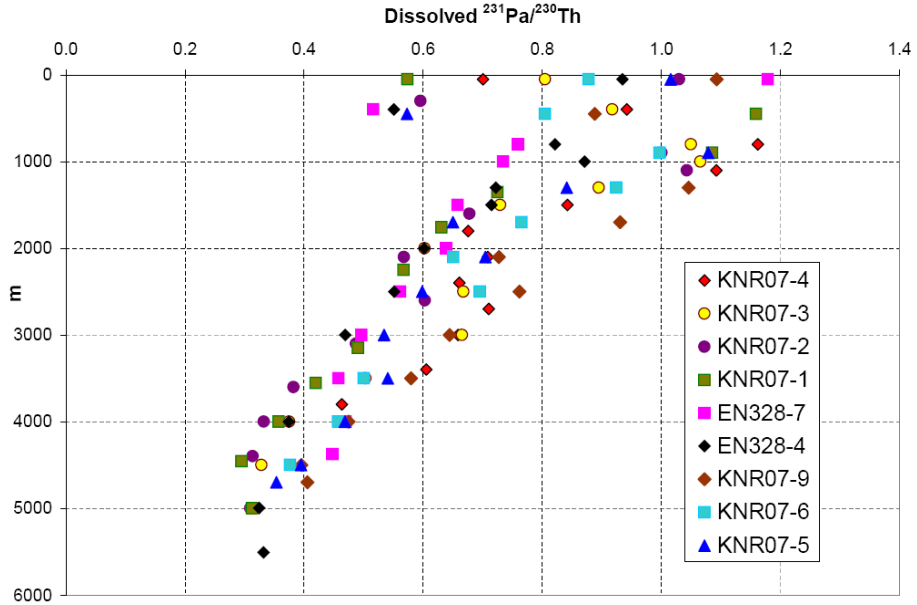

Fig. 12. Dissolved $^{231}Pa/^{230}Th$ profiles measured at 9 stations in the North and Equatorial Atlantic (Table 2).

OSD

6, 2755–2829, 2009

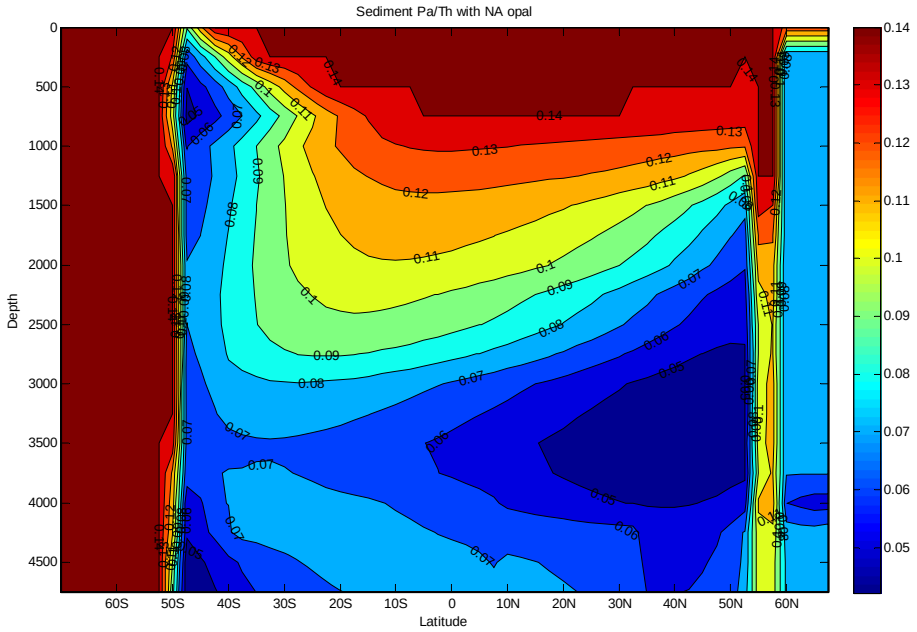

Fig. 13a. **(a)** Sediment $^{231}Pa/^{230}Th$ generated with an opal belt just south of the site of deep water formation. **(b)** Difference in the sediment $^{231}Pa/^{230}Th$ field generated in with and without the northern opal belt.

OSD
6, 2755–2829, 2009

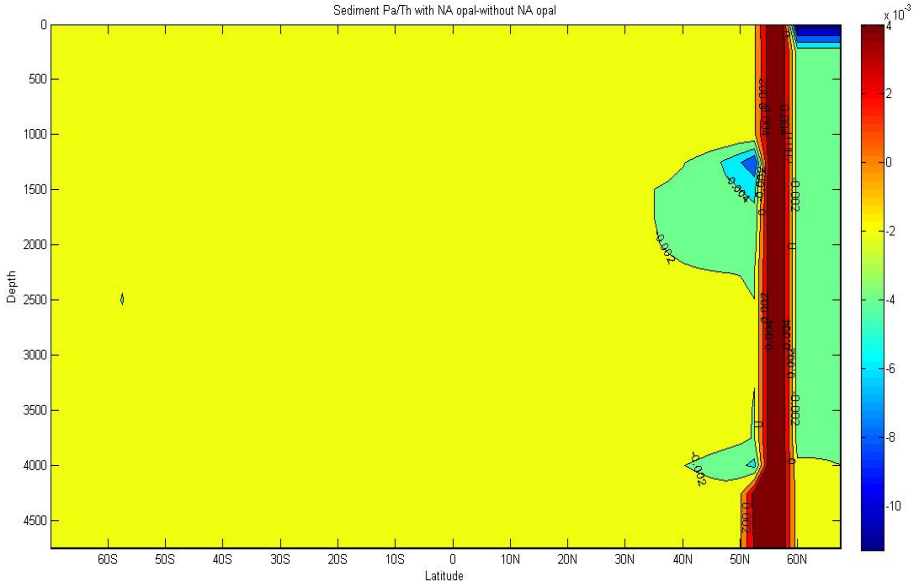

Fig. 13b. Continued.

OSD

6, 2755–2829, 2009

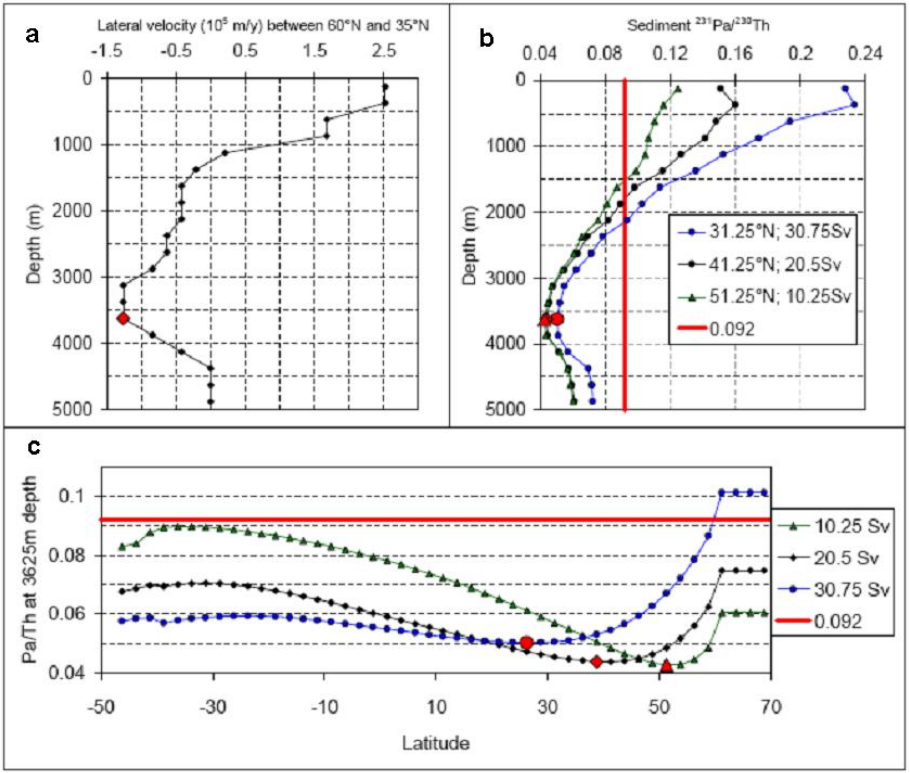

Fig. 14. (a) Lateral velocity profile in the control run between 60° N and 35° N. **(b)** Vertical sediment ^{231}Pa/^{230}Th bathymetric profiles generated by the model at different rates of overturning and at the latitude where the lowest sediment ^{231}Pa/^{230}Th is found. **(c)** Latitudinal sediment ^{231}Pa/^{230}Th profiles for different rates of overturning at the depth where the lowest sediment ^{231}Pa/^{230}Th is found (3625 m).

OSD
6, 2755–2829, 2009

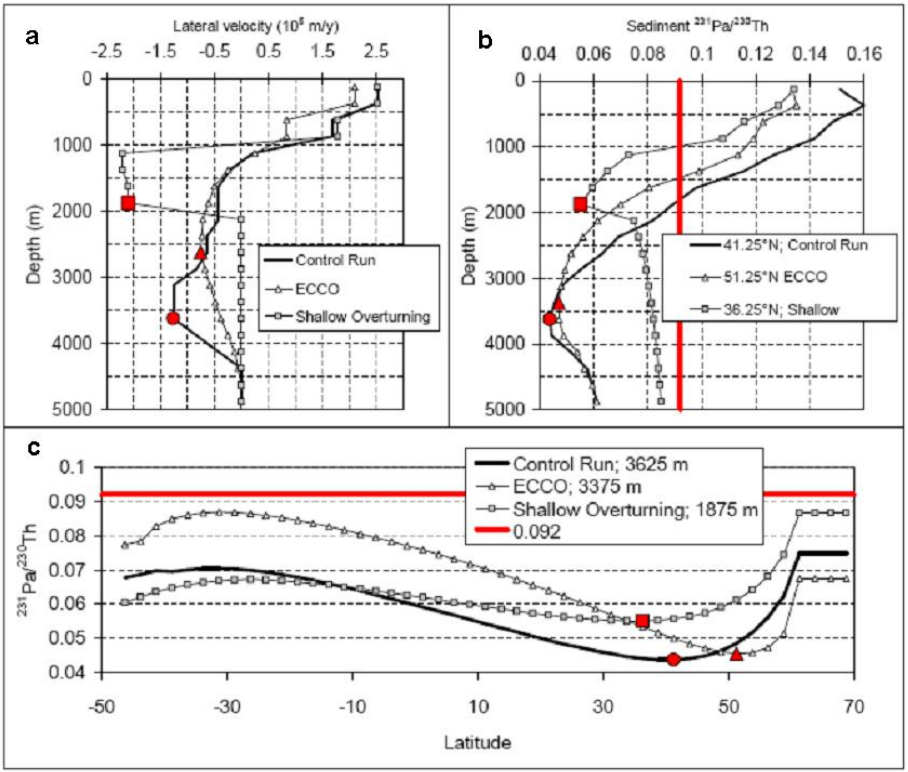

Fig. 15. (a) Contrasting lateral velocity profiles between the control run (20.5 Sv), the overturning profiles from the ECCO consortium (14 Sv; Wunsch and Heimbach, 2006) and an arbitrary shallower overturning cell (20.5 Sv). **(b)** Vertical sediment ^{231}Pa/^{230}Th bathymetric profiles generated by the three overturning profiles at the latitude where the lowest sediment ^{231}Pa/^{230}Th is found. **(c)** Latitudinal sediment ^{231}Pa/^{230}Th profiles generated by the three overturning cells at the depth where the lowest sediment ^{231}Pa/^{230}Th is found.

OSD
6, 2755–2829, 2009

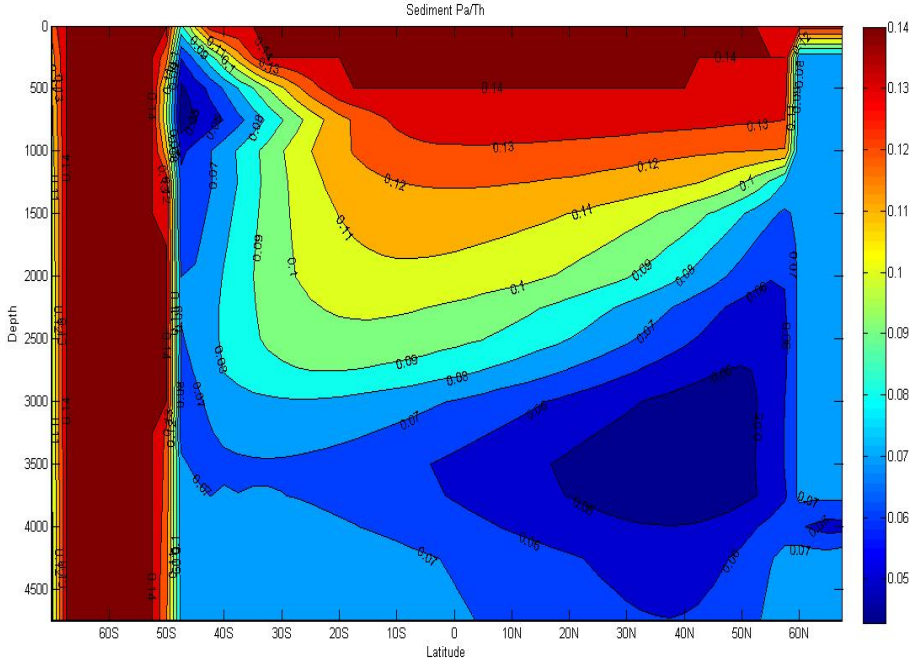

Fig. 16. Sediment $^{231}Pa/^{230}Th$ field generated in the control run without formation of AABW.

OSD

6, 2755–2829, 2009

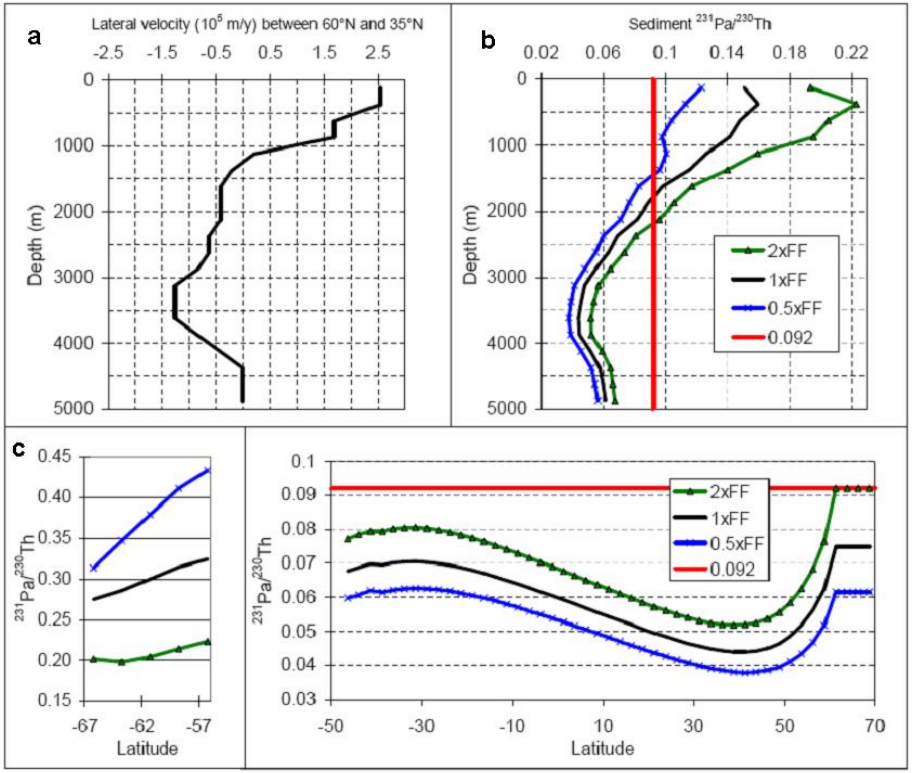

Fig. 17. The influence of Southern Ocean fractionation factor on the sediment ^{231}Pa/^{230}Th in Atlantic sediments. **(a)** Lateral velocity field used to conduct the experiments. **(b)** Vertical sediment ^{231}Pa/^{230}Th gradient generated by the control run (1xFF) and when the Southern ocean equilibrium fractionation factor (FF=0.9) is doubled (2xFF) or halved (0.5xFF). **(c)** Sediment ^{231}Pa/^{230}Th produced in the North Atlantic and the Southern Ocean under these three scenarios.

OSD
6, 2755–2829, 2009